# HEAT FLUX CHARACTERISTICS OF SPRAY WALL IMPINGEMENT WITH ETHANOL, BUTANOL, ISO-OCTANE, GASOLINE AND E10 FUELS

**J. Serras-Pereira and P.G. Aleiferis***

Department of Mechanical Engineering, University College London, UK

**H.L. Walmsley, T.J. Davies and R.F. Cracknell**

Shell Global Solutions (UK), Ltd., Thornton, UK

*Author for Correspondence:

Dr. Pavlos Aleiferis

University College London

Department of Mechanical Engineering

Torrington Place, London WC1E 7JE, UK

Tel: +44-(0)20-76793862, Fax: +44-(0)20-73880180

E-mail: p.aleiferis@ucl.ac.uk

*Full length article accepted for publication in the International Journal of Heat and Fluid Flow.*

**ABSTRACT**

Future fuel stocks for spark-ignition engines are expected to include a significant portion of bio-derived components with quite different chemical and physical properties to those of liquid hydrocarbons. State-of-the-art high-pressure multi-hole injectors for latest design direct-injection spark-ignition engines offer some great benefits in terms of fuel atomisation, as well as flexibility in in-cylinder fuel targeting by selection of the exact number and angle of the nozzle's holes. However, in order to maximise such benefits for future spark-ignition engines and minimise any deteriorating effects with regards to exhaust emissions, it is important to avoid liquid fuel impingement onto the cylinder walls and take into consideration various types of biofuels. This paper presents results from the use of heat flux sensors to characterize the locations and levels of liquid fuel impingement onto the engine's liner walls when injected from a centrally located multi-hole injector with an asymmetric pattern of spray plumes. Ethanol, butanol, *iso*-octane, gasoline and a blend of 10% ethanol with 90% gasoline (E10) were tested and compared. The tests were performed in the cylinder of a direct-injection spark-ignition engine at static conditions (*i.e.* quiescent chamber at 1.0 bar) and motoring conditions (at full load with inlet plenum pressure of 1.0 bar) with different engine temperatures in order to decouple competing effects. The collected data were analysed to extract time-resolved signals, as well as mean and standard deviation levels of peak heat flux. The results were interpreted with reference to in-cylinder spray formation characteristics, as well as fuel evaporation rates obtained by modelling. In addition, high-speed images of single droplets of fuel impinging onto the array of the heat flux sensor were acquired with simultaneous sampling of the heat flux signal in an attempt to provide further interpretation. The single droplet tests showed ability of the signals to quantify droplet mass impinged on the sensor. Analysis of the peak heat flux at static engine conditions quantified values of fuel temperature at impingement in agreement with the wet bulb temperatures predicted by the droplet evaporation model. Comparison of the static and motoring engine heat flux signals around the bore showed the effect of the intake flow on the spray's pattern at impingement and demonstrated fuel presence on the liner that survived at exhaust valve open timing. The general behaviour was different for the alcohols to that of the hydrocarbons, with ethanol exhibiting the effect of its high latent heat on the signals and butanol exhibiting effects related to poor atomization and slow evaporation.

**NOMENCLATURE**

| | |
|---|---|
| $d$ | Diameter |
| $\mu$ | Dynamic Viscosity |
| $p$ | Pressure |
| $p_A$ | Ambient Pressure |
| $r_0$ | Initial Radius of Fuel Droplet |
| $Re$ | Reynolds Number |
| $\rho$ | Density |
| $\sigma$ | Surface Tension |
| $T$ | Temperature |
| $T_A$ | Ambient Temperature |
| $T_0$ | Initial Droplet Temperature |
| $u$ | Velocity |
| $We_L$ | Weber Number, Liquid Phase |

**ABBREVIATIONS**

| | |
|---|---|
| ADC | Analogue to Digital Converter |
| AFR | Air-to-Fuel Ratio |
| ASOI | After Start Of Injection |
| ATDC | After intake Top Dead Centre |
| BDC | Bottom Dead Centre |
| CA | Crank Angle |
| COV | Coefficient Of Variation |
| DISI | Direct Injection Spark Ignition |
| EVC | Exhaust Valve Closure |
| EVO | Exhaust Valve Open |
| HC | unburned Hydro-Carbons |
| HFS | Heat Flux Signal |
| IVC | Intake Valve Closure |
| IVO | Intake Valve Open |
| PDA | Phase Doppler Anemometry |
| PFI | Port Fuel Injection |
| RMS | Root Mean Square |
| RPM | Revolutions Per Minute |
| RTS | Resistance Temperature Sensor |
| SI | Spark Ignition |
| SMD | Sauter Mean Diameter ($D_{3,2}$) |
| SOI | Start of Injection |
| TDC | Top Dead Centre |
| UNIFAC | UNIversal quasichemical Functional group Activity Coefficient |

## INTRODUCTION

### BACKGROUND

Understanding the effect of bio-components on fuel spray formation is an essential challenge, especially in the context of latest design Direct Injection Spark Ignition (DISI) engines that are very sensitive to fuel properties. Fuel spray wall impingement has been a common issue for the previous generation of Spark-Ignition (SI) engines that were operated by Port Fuel Injection (PFI) systems. Traditionally this resulted in problematic transient control related to time lag from fuel films deposited on the surfaces of the engine's intake port and altered the in-cylinder A/F Ratio (AFR) [1, 2]. The development of DISI engines brought the problem of fuel films on surfaces from the engine's intake port into the engine's cylinder like in Diesel engines [3]. DISI engines operate with injection pressures of 150–200 bar or more in order to provide efficient fuel atomisation and mixture formation over a wide range of engine operating conditions. However, this can lead to direct spray impingement onto the piston crown and liner, leading to a deteriorating effect on the engine's exhaust emissions, especially unburned Hydro-Carbons (HC) and Particulate Matter (PM). Considering strict pending emissions regulations, liquid fuel wall impaction should be minimised in DISI engines. This requires fundamental understanding of many physical processes, including spray formation, flow interactions and the effect of fuel properties. Such understanding has been traditionally sought by simplified experiments on individual droplets in an attempt to describe the behaviour of sprays and the outcome of spray impingement under controlled conditions, despite the known fact that dense sprays in engines do not really behave as a summation of individual droplets. A literature review addressing this issue has been published recently [4], therefore this introduction will not elaborate further on describing relevant phenomena and physical mechanisms of droplet wall impaction and heat flux. However, it is noted that there are very few reports in the literature that have dealt with *in-situ* measurements of liquid films on the piston and liner surfaces of DISI engines. Typical examples of such work are Phase Doppler measurements or Laser Induced Fluorescence (LIF) visualisation, *e.g.* [5] with *iso*-octane and [6–10] with gasoline. The measured fuel films were of different size among these researchers, especially for the two different fuels, typically 10 μm for *iso*-octane and 45 μm for gasoline. However, the differences in the injection systems, engines and conditions used by these studies, as well as uncertainties related to calibration of LIF signals, preclude widely applicable conclusions to be made. Drake *et al.* [11] developed a high-speed refractive-index-matching imaging technique for time/space-resolved measurements of fuel mass on the quartz piston window of an optical DISI engine over a range of stratified-charge conditions with both a pressure-swirl atomiser and a multi-hole injector. The fuel-film mass was typically found to be a fraction of 1% of the total fuel injected (maximum of ~1% with gasoline and ~0.1% with *iso*-octane) with the pressure-swirl injector, whilst use of the multi-hole injector reduced this further by a factor of 10. Camacho and Hall [12] used a piezoelectric sensor to measure the mass of fuel that impacted on the piston crown of a DISI engine. Gasoline was delivered by a vertical swirl injector and aimed at the centre of the piston. The injection pressure was quite low (5 bar), and the fuel was injected over a long period of time under motored engine conditions (11° CA at 600 RPM, 0.69 bar intake pressure). The measured fuel mass on the sensor surface was typically less than 2 mg, which corresponded to a film height of 32 μm. The maximum measured mass for stoichiometric operation with late injection was 2.3 mg at TDC and corresponded to 6.3% of the fuel injected. This percentage was very large considering the ratio of sensor to

piston areas, suggesting that the majority of the injected fuel became a liquid fuel film. Near Bottom Dead Centre (BDC) the mass of the fuel film did not reach values higher than 0.5 mg (8 μm in height).

Other methods of measuring fuel impingement on engine surfaces have involved use of heat flux diagnostics [13–16]. Specifically, Shayler *et al.* [13–15] used surface mounted heat flux sensors in the intake port of a PFI gasoline engine to investigate the heat transfer between the wall film and the surrounding gas phase. The signals showed peaks in the heat flux when impingement occurred initially soon after fuel injection and then a second peak later in during the intake stroke due to rapid evaporation associated with backflow into the intake ports. The highest levels of heat flux were recorded for cold engine conditions, suggesting that little fuel evaporation took place initially on impact with the port walls. It was also found that at fully warm conditions, the signal for *iso*-octane was higher and disappeared more rapidly than for gasoline. This was considered evidence that gasoline's heavy fractions remained on the sensor for longer, evaporating during the remainder of the intake stroke and thus contributing to the higher heat flux signal recorded for this period. At cold conditions, the signals for the two fuels were found to be very similar. In similar methodology to that of [13–15], heat flux signals for dry conditions, using propane, and wet conditions, using isooctane, were obtained in [16] and their difference was used to calculate the net heat transfer. This value was considered to be the sensible and latent heat required to heat and vaporise the impinging fuel. Reasonable results were reported apart from at high wall temperatures where other heat transfer modes made estimation more difficult.

No detailed work was found in the literature that has investigated direct fuel spray impingement onto the liner of latest geometry DISI engines with centrally mounted multi-hole injectors. Furthermore, there is absence of knowledge on the in-cylinder dynamics of new fuels that will include bio-derived components. Gasoline already contains 5% ethanol (E5) in many countries and is compatible with existing combustion systems but there is pressure for the ethanol content to increase, with some markets demanding much higher proportions (E85 or even E100). However, not all components on the vehicle are necessarily compatible with blends containing large amounts of ethanol. At the other end, the vapour pressure of blends with intermediate percentages of ethanol, *e.g.* E10, is higher than the vapour pressure of either ethanol or gasoline because the mixture deviates from the ideal solution behaviour (Raoult's law). This deviation significantly alters the distillation curve of the blend in comparison to that of pure gasoline [17, 18]. Other alkyl alcohols, such as butanol, have also been suggested as possible gasoline components. Having twice as many carbon atoms as ethanol, butanol is more hydrocarbon-like in its properties. However, butanol lags behind ethanol in terms of commercial production.

## PRESENT CONTRIBUTION

There are very limited experimental data which demonstrate the role that liquid fuel transport properties can have on spray wall impingement in DISI engines. The main objective of the current work has been to investigate the heat flux technique using specific steps. In particular, monodisperse fuel droplet impingement on the sensor's surface was initially imaged to understand the response of the heat flux signal at 1.0 bar atmospheric conditions. Then the extent of fuel wall impingement and heat flux at key in-cylinder locations under 'static' engine conditions, *i.e.* in the engine's quiescent cylinder at 1.0 bar, was studied. This was done to decouple the effects of spray-flow interactions and isolate at first approximation the effect of fuel properties on spray formation and impingement heat flux. This heat flux was measured with a range a multi-component

gasoline, *iso*-octane, ethanol and butanol, as well as a low-content ethanol/gasoline blend (E10). Finally, heat flux data were acquired with the engine running at 1500 RPM with 1.0 bar intake pressure to examine the effect of in-cylinder flow on spray wall impingement for all fuels. The development and application of the heat flux sensing diagnostic technique was done from a perspective that such measurements do not exist in the literature, although essential for engine modellers and for fundamental understanding of in-cylinder processes. They can allow useful insights into phenomena without the recourse to optical diagnostics methods which are far more difficult to apply routinely, quantitatively and cost-effectively in realistic engine environments. The paper makes an attempt to discuss the benefits and practical problems in as a clear and self-contained manner as possible.

## EXPERIMENTAL APPARATUS AND PROCEDURE

### RESEARCH ENGINE

A single-cylinder optical DISI engine with pentroof combustion chamber was used to investigate the spray behaviour within the confinements of the cylinder walls. The engine had a bore of 89 mm and a stroke of 90.3 mm (562 $cm^3$) with a compression ratio of 11.15; more details about the engine can be found in previous publications by the current authors on in-cylinder spray dynamics and combustion [19–21]. The influence of engine temperature was observed using controlled engine-head coolant temperatures of 20 °C, 50 °C and 90 °C. Enough heat-soak time (30–40 min) was allowed at all temperatures so that the engine head and liner components acquired enough thermal inertia to simulate cold, semi-warm and fully warmed-up conditions. Under such conditions, the engine head temperature was also considered to be a measure of the temperature of the fuel that was sitting in the injector that was installed centrally in the engine head. Synchronization of various control triggers for injection and data acquisition was achieved by use of an AVL engine timing unit.

### INJECTOR

A multi-hole injector originally designed for vertical installation in a DISI engine head in close spacing arrangement with the spark plug was used for this investigation. The injector had six nozzle holes in an asymmetric arrangement with respect to the vertical axis. **Fig. 1** shows a schematic of the injector and its spray plumes through two views. Plumes #1 and #6 had a 58.5° inclination with respect to the vertical axis and have been designed to pass on either sides of the spark plug *i.e.* one at the intake side and the other at the exhaust side of the engine. More details about the injector geometry, nozzle-hole angles and spray formation characteristics can be found in previous studies of spray formation by the current authors [22–26].

### FUELS

Five fuels were investigated: a typical commercial grade gasoline (RON95), *iso*-octane, butanol, ethanol and E10 (blend of 10% ethanol with 90% gasoline). A standard commercial grade European gasoline contains several hundred hydrocarbons, typically about 25–30% C5 or lower, 30-40% C6–C8 and the remainder C9–C10 hydrocarbon chains. *Iso*-octane is a single component of gasoline with a boiling point of 99 °C at 1 bar; butanol boils at 117°C while ethanol boils at 78.4°C. E10 was also selected as a fuel to test because the vapour pressure of E10 is higher than the vapour pressure of either ethanol or gasoline and the distillation curves of those two fuels in **Fig. 2** reflect clearly this effect; E10 was blended specifically for this work by the petrol manufacturer co-authoring this work and the gasoline part of E10 was the same to the pure gasoline tested.

**Fig. 2** also shows the boiling points of the single-component fuels that were tested (as vertical lines). **Table 1** shows a number of selected fuel properties which are relevant to spray formation and evaporation characteristics at 1 bar.

HEAT FLUX MEASUREMENTS

Fast-response small heat flux sensors made by Vatell were used for the present investigation; specifically, a heat flux sensor of type HFM-7 was used in conjunction with an amplifier of type AMP-6 [27]. This sensor is based on thermocouple technology and essentially joins many thermocouple pairs in series to form a flat plate differential thermopile. Two types of measurement are made simultaneously. The first is a temperature measurement from a Resistance Temperature Sensor (RTS) element, consisting of a thin film deposited in a loop pattern around the outer edge of the sensor face. The second is a Heat Flux Sensor (HFS) measurement from the thermopile that is 6.4 mm in diameter and occupies most of the surface area on the sensor face. This is not equivalent to a thermocouple signal; it acts as a differential source and therefore is not grounded. When heat flows into or out of the substrate surface, a small temperature difference develops across the thermal resistance elements of the thermopile, and each thermocouple pair produces a voltage proportional to the heat flux. The total voltage across the thermopile is the sum of these voltages, and indicates the direction and magnitude of the heat flux.

The total thickness of the thin film which makes up the sensor is less than 2 μm; as a result, the response time of the sensor is of the order 17 μs if used uncoated as shown in **Fig. 3**. **Table 2** lists the sensor's details. From the amplifier calibration report, a gain setting of 500 corresponded to a bandwidth of 50 kHz for both HFS and RTS channels. After initial tests, a gain of 500 was found to be compatible with the range of signal levels obtained relative to the ±6 V full scale output from the amplifier and was adopted for all test conditions. The amplifier gain accuracy for this setting was ±1.5 % for both the HFS and the RTS channels. The signals were both digitised with a 12-bit ADC data acquisition card within a Labview environment and logged with a sampling rate of 45 kHz. The digitisation error was reduced to a minimum by adjusting the voltage range over which the 12 bits were used. Signal amplitude was in the range –6.0–4.0 V for high signals and as low as ±1 V for very small signals.

Once logged, the signals required processing in order to obtain the final heat flux and temperature measurements. To this end an algorithm was coded in MATLAB to batch process the high volumes of data and to output relevant parameters and statistics, *e.g.* the magnitude and timing of the peak recorded heat flux for each injection, their mean and Coefficient of Variation COV (standard deviation/mean) values, *etc.* The RTS measurement was critical to proper heat flux measurement because the HFS was temperature dependent. The RTS relied on the fact that the thin film resistance changed as a function of temperature. This function was described by a cubic polynomial function, characterized for each sensor by the manufacturer. Once the temperature was known, the heat flux could be computed using voltage and gain via calibration sheets produced by the manufacturer. More details on the method can be found in [28], where high-speed imaging of in-cylinder spray impingement, along with an initial set of heat flux data under low-load engine running conditions (0.5 bar intake pressure), were obtained to identify typical locations of fuel wall impingement.

ENGINE INSTALLATION OF HEAT FLUX SENSORS

A ¼ stroke short steel cylinder liner ring was designed to house the heat flux sensors and be used with a ¾ stroke water-cooled cylinder liner. The advantage of having a removable ring in which to insert the heat flux sensors was that it gave effectively infinite flexibility of sensor location around the cylinder. The steel ring was machined with multiple inserts to cope with simultaneous heat flux sensors mounted flush with the cylinder wall; however, only one sensor was used throughout the current study (*i.e.* the ring was rotated to sweep various 'polar' locations of measurement as will be discussed later). The sensor was secured with a capture nut, which was designed and manufactured in-house and then shipped to the manufacturer to be integrated with the HFS micro-connector assembly. This was necessary due to the particular micro soldering requirements of the assembly and subsequent calibration procedure, which could only be carried out by the manufacturer. The steel ring with a heat flux sensor installed is shown in **Fig. 4**. The main purpose of this arrangement was to allow investigation of the region around where plumes #1 and #6 were expected to impinge, as a result of the injector nozzle angles and orientation in the combustion chamber (shown in **Fig. 1**). The placement of the sensors was defined by spray imaging tests carried out at different planes along the length of the cylinder liner, in order to identify the most severe locations of impingement around the bore; the final plane selected was 17 mm below the head gasket and based on that dimension the steel ring was designed and installed in the engine with the heat flux sensors in place.

To bring the wall heat-flux measurements and in-cylinder spray phenomena into perspective and to give the reader a visual aid of reference for the general locations of spray impingement around the cylinder's liner, **Fig. 5** shows an image of a typical *iso*-octane spray produced under static engine conditions at 20 °C (*i.e.* into the engine's quiescent cylinder at 1.0 bar). The image has been overlaid with a polar grid set whose origin has been located at the centre of the optical piston crown window (hence centre of the cylinder bore). The image corresponds to Mie scattering that was captured by Laser-sheet illumination on the horizontal plane of the heat flux sensors. For more details on the spray imaging arrangement the reader is guided to [28, 29], as analysis of spray formation from images is not central to the current paper. Initial location sweeps around 140° of the cylinder bore at 10° increments were used to obtain heat flux measurements for different engine head coolant temperatures. The heat flux sensor ring was clamped in place and the cylinder liner operated with the same coolant temperature as the engine head for the majority of the tests, typically at 20 °C, 50 °C and 90 °C. Some tests were also carried out with the engine head temperature fixed at 20 °C and the liner temperature varied in the range 10–90 °C.

The heat flux tests were done initially whilst the engine was not running, *i.e.* in static quiescent engine environment at 1.0 bar, in order to obtain reference/benchmark impingement conditions with effects of in-cylinder air-flow motion decoupled from spray development. Subsequently, the tests were repeated whilst the engine was motoring on the dynamometer at 1500 RPM with 1.0 bar intake pressure (*i.e.* wide-open-throttle operation), for direct comparison with the static engine conditions at 1.0 bar. For the static tests the piston was removed so that repeated injections could be made without the build up of fuel vapour inside the engine's chamber. Based on previous work by the current authors [19, 20], an injection strategy early in the intake stroke was used for 'homogeneous' mixture formation; the Start Of Injection (SOI) was set to 80 °CA After intake TDC (ATDC) and the injection pulse width was 0.8 ms (approximately 7.2 °CA at 1500 RPM).

At static engine conditions the range of sensor location sweeps was set to cover the main impingement locations and ranged from -30°–+55° in 5° increments. After extensive testing with various frequencies of injection, a frequency of 1 Hz was adopted for all static engine measurements. This duty cycle was selected because, in combination with the injection duration of 0.8 ms that was used with all fuels, injection frequencies higher than 1 Hz indicated fuel accumulation on the sensor's array that decreased the sensitivity of the sensor. More specifically, sensitivity issues were investigated by injecting different amounts of fuel (using longer pulse widths) and by using different time delays between individual injections. Longer injections were found to have a 'damping' effect on the peak signals as a result of the remaining unevaporated fuel films from previous injections acting as a thermal barrier for heat transfer. Similarly, increasing the frequency of injection also had a damping effect as there was not enough time available between injections to evaporate the fuel film off the sensor face at 20 °C fuel temperature, sensor temperature and ambient temperature. This effect reduced significantly with increasing sensor and fuel temperature and was typically smaller for the higher volatility fuels. Imaging also showed how the whole area of the sensor was in contact with fuel upon impingement; tests were also carried out to examine this by masking parts of the sensor and studying the signal.

Furthermore, droplet evaporation modelling (based on methods discussed in later section) showed that for gasoline, *iso*-octane, ethanol and E10, droplets of 50 μm in size and of temperature in the range 20–90 °C, took less than ~0.2–0.3 s to evaporate in 20 °C air when travelling at speeds of 50 m/s (even for droplets of the same size but with speed of 0 m/s, evaporation was complete by 0.5 s). Considering that droplet sizing measurements of the same injector by the current research group [30] had shown values of Sauter Mean Diameter (SMD) in the range of 10–35 μm 25 mm downstream the injector nozzle (travelling at 30–40 m/s), the 1 Hz injection frequency was considered an adequate timescale within theoretical and practical reasoning. The modelling also showed that for butanol, *i.e.* the fuel with highest single boiling point, the predicted timescale of evaporation for 50 μm droplets was ~0.7–0.9 s, *i.e.* quite close to the 1 s separation between injections; however, it was decided to keep the frequency of injection at 1 Hz for butanol too in order to examine effects in direct comparison to the other more volatile fuels.

All injection set points were repeated under motoring engine conditions at 1500 RPM (*i.e.* with an injection frequency of 12.5 Hz). The sensor location sweeps were adapted to cover the main impingement locations under motoring and ranged from -30°–+90° in 10° increments. The optimum number of injections for static and motoring engine conditions was identified on the basis of the COV of peak heat flux; the latter achieved steady-state values at ~100 injections for static conditions and at ~200 cycles for running engine conditions, hence typically a minimum of 100 and 200 events were acquired, respectively.

## SINGLE DROPLET IMPINGEMENT

To analyse the performance and signal characteristics of the heat flux sensor at idealised conditions of liquid droplet impingement, the heat flux signal produced at impingement by fuel droplets free-falling in a quiescent environment at 1.0 bar, 20 °C, from a distance of 50 mm above the sensor face was analysed by imaging. A solenoid activated single-droplet generator was used to produce isolated free falling fuel droplets under controlled conditions. The droplets selected for all tests presented in this paper were 300 μm in nominal diameter. This size was representative of the diameter of the injector's nozzle holes [24–26]. The droplet at the point of release was at 20 °C and the temperature of the heat flux sensor onto which the droplet was impacted

was controlled for tests in the range 20–90 °C. The fuel selected for the experiments in the current paper was *iso*-octane. However, the alcohols were also tested and it needs to be noted that certain properties of those fuels presented some challenges and practical problems whose analysis is beyond the scopes of the current paper, *e.g.* use of butanol resulted in droplets of certain size bouncing off the sensor's array and away upon impingement (from viscosity/surface tension effects). Those issues will be studied and discussed in a future publication. A high-speed camera (Photron APX-RS) was employed to record individual events of droplet impingement onto the heat flux sensor; a frame rate of 9 kHz was used, *i.e.* one image taken every 0.111 ms. The camera had on board memory of 2.14 GB which allowed continuous acquisition of 6826 greyscale images at 640×480 resolution. Typically 100 individual impaction events were acquired and stored in series of 8-bit Tagged Image File Format (TIFF) files. Simultaneous acquisition of heat flux traces and their analysis was done within Labview and MATLAB using the same methods to those employed for the in-cylinder impinging sprays.

## RESULTS AND DISCUSSION

### HEAT FLUX OF SINGLE DROPLET IMPINGEMENT

#### *General Characteristics*

Imaging and heat flux measurements of *iso*-octane droplets at 20 °C liquid temperature, impacting on the heat-flux sensor face which was also at 20 °C, are discussed here. The initial temperature drop arising from the transient phase of evaporation as the droplet fell to its wet-bulb temperature resulted in a negative heat flux on first impact with the sensor. **Fig. 6** shows a four-image sequence of a falling droplet of 300 μm and a subsequent secondary 'satellite' droplet of 180 μm which occurred due to a rare event related to the performance of the droplet generator system; this sequence was specifically selected to demonstrate the sensitivity of the heat flux sensor. The corresponding graph in **Fig. 6** shows the sharp response of the heat flux signal as the droplet impacted onto the sensor face. The smaller satellite droplet was also registered as a smaller negative local peak value after the main droplet impact. This indicated that the heat flux system was sensitive to mass levels under certain conditions because the $\Delta T$ for both droplet impact events was essentially the same (from calculations of wet-bulb temperature). The smaller absolute value of peak voltage registered for the smaller droplet was related to the smaller area that this droplet spread over due to the different number of thermocouple connections that it came in contact with, *i.e.* the sum of voltages that defined the sensor response was lower than for the larger droplet. The fact that the satellite droplet fell on the edge of the main droplet also resulted in a thermal barrier to this second heat transfer event, contributing further to a lower peak heat flux for this impingement process.

The main droplet impact event was inspected in greater detail and the time development of the sensor's signal is shown against corresponding images of the droplet's impact event in **Fig. 7**. The heat flux sensor was found to exhibit significant sensitivity to the fluid dynamics of droplet impact. Initially the signal started at 'zero' level as the system was in thermal equilibrium; a sharp drop then started to occurred at around sample number #853 (where 1 sample=16.67 μs) as the droplet first came in contact with the sensor upon impact and the 'first' heat flux was recorded. As some of the droplet mass rebounded into a thin cone at sample #866, the sensor's signal also reacted, demonstrating great sensitivity to very small changes in the droplet's dynamics. As the

droplet finally spread out, *e.g.* at sample #872, the heat flux signal reached a maximum, indicating again that the area over which heat transfer occurred affected the total voltage output of the sensor. In the final image, residual momentum and elasticity in the fuel film from the droplet impact still caused the heat flux signal to respond accordingly (sample #890).

The single droplet generator was also used to benchmark the shot-to-shot variability of the peak heat flux produced for otherwise repeatable droplet impact events. For a series of 100 droplet impact events taken within an interval of 5 s each and with the droplet generator producing reliably droplets of 300 μm ±20μm, the COV of the peak heat flux signal was found to be ~15%.

Finally, the droplet generator was used to check whether the imaged droplet evaporation time corresponded to the time taken for the heat flux signal to return to zero levels. For this test, the sensor was mounted in an aluminium plate and heated to 90 °C to increase the evaporation rate. As shown in **Fig. 8**, the total evaporation time was found from the heat flux signal to be 276.5 ms (±1.6 ms). The images revealed that complete droplet evaporation was over in 278.3 ms after impact (±500 μs). This test showed that it was possible therefore to use the heat flux signal to determine the presence and disappearance of a fuel film on the sensor surface with good accuracy.

*Mass Estimation*

Having assessed the signal response to single droplet impingement events, the integral of the signal was used to estimate the droplet mass evaporated from the sensor's face from a single impingement event (the integral of the signal typically corresponds to the sensible and latent heat required to heat and vaporise the impinging fuel). The droplet impact event of **Fig. 8** was used to test this methodology. The value of the integral was multiplied by the equivalent area over which the heat transfer from the droplet to the sensor thermopile actually took place *i.e.* the contact area of heat transfer measurement based on dimensions of the thermopile array wires provided by the manufacturer of the sensor. The high-speed images were meticulously examined to establish how the droplet spread on impact. It was found that the droplet was in contact with 5 separate thermopile traces during the first 65% of its evaporation time. From 65%–90% of the evaporation time, the film formed by the droplet reduced in size and covered 3 thermopile traces; in the last 10% of the droplet's lifetime, the film was in contact only with 1 thermopile trace. The obtained value of energy was then transformed to mass using *iso*-octane's heat properties and compared to the actual mass of the *iso*-octane droplet calculated from is known size, volume and density. The difference between the calculated mass of the 300 μm droplet and the estimated value from the heat flux signal was found to be only ~1.3%. This analysis indicated that the system was able to respond quantitatively to levels of fuel mass impinged.

## DROPLET EVAPORATION MODELLING

Before carrying the work over to in-cylinder fuel injection and in order to have a baseline for examining whether the heat flux signals were proportional to the $\Delta T$ of the wall impinging fuel spray droplets and sensor, a transient single droplet evaporation model was used to simulate wet-bulb temperatures and droplet evaporation rates for all the fuels tested at different initial states relevant to the injector and engine conditions. The model used a Redlich-Kwong equation of state based on UNIFAC method coefficients for each species identified on the gas chromatograph of each of the fuels. It also solved a transient single-component evaporation model of the type presented by Faeth [31] but represented multi-component behaviour by using

property data that varied with fraction evaporated and temperature. During evaporation, the property data for the remaining fuel in the droplet was continually re-calculated by linear interpolation from values in lookup tables that gave the properties as a function of temperature and fraction evaporated. The evaporation part of the model first performed an adiabatic flash calculation to get the vapour pressure of the droplets down to the system pressure. Then the transient heat and mass transfer models were solved simultaneously to follow the evaporation process. The model assumed good mixing and heat transfer within the liquid droplets so that the composition and temperature were uniform. The droplet velocity had no influence on the temperature versus fraction evaporated but, like the droplet size, it had great influence on the rate of evaporation and temperature change in time. The velocity of the droplet decreased with time due to drag; this was dealt with by a Reynolds number correlation [32].

The model was run for initial droplet conditions typical of the spray breakup produced by the current injector. Specifically, average droplet sizes and velocities measured by Phase Doppler in a quiescent injection chamber for the exact same injection system were of the order 10–35 μm and 30–40 m/s, respectively, 25 mm downstream of the injector's nozzle within plumes #1 and #6 [30], *i.e.* at about half way from the point of injection to the point of in-cylinder wall impact at static engine conditions. These values give a liquid Weber number ($We_L=\rho_L u^2 d/\sigma$) of the order 400 and a Reynolds number ($Re=\rho_L u d/\mu_L$) of the order 600 (the latter similar to that of the monodisperse droplet experiment discussed earlier). Spray tip plume penetration velocities were as high as ~80 m/s, depending on conditions and fuel type [30]. Considering those data, a 50 m/s relative velocity was selected to simulate evaporating droplets within the scopes of the current paper. Taking into account that the injection nozzle had an inner diameter of 200 μm and an outer diameter 500 μm to avoid coking effects (the reader is guided to [25, 26] for detailed analysis of the nozzle's geometry), and that that break-up mechanisms can also lead to large ligaments/droplets with size of the same order to the nozzle's diameter when close to the nozzle's exit, a droplet diameter of 50 μm was elected as initial condition.

Graphs of 'droplet fraction evaporated' and 'droplet surface temperature' are shown in **Fig. 9** for ambient conditions of $p_A$=1.0 bar and $T_A$=20 °C, concentrating on the early stage of evaporation of 2 ms (equivalent to 18° CA at 1500 RPM in reference to the graphs of heat flux). Initial droplet temperatures ($T_0$) were varied in the range 20–120 °C. The lowest droplet temperatures during evaporation were achieved for all fuels within the 2 ms timescale and summarised in **Table 3**. For single-component fuels like *iso*-octane, the maximum temperature depression applied approximately throughout the early quasi-steady evaporation period of ~2 ms and then remained approximately constant for the rest of the evaporation. Higher initial fuel temperatures increased the wet-bulb temperature for the multi-component fuels as a result of initial 'flashing off' of the high volatility components. For those fuels the peak temperature depression occurred early in the evaporation process (typically within 2 ms, while the initial liquid temperature still had some influence), but then the depression declined markedly from the maximum as the evaporation proceeded past 2 ms (the latter behaviour is not shown in **Fig. 9** due to the elected cut-off scale of 2 ms on the horizontal axis). Sensitivity tests showed that the droplet size had no influence on the temperature versus fraction evaporated (mass and heat transport both scaled in the same way with droplet size) but it strongly influenced the timescale for evaporation; smaller droplets evaporated much faster than larger ones but sensitivity test showed that the exact initial droplet size

was not critical with respect to general trends between fuels which was the main objective of this modelling exercise.

## SPRAY WALL IMPINGEMENT HEAT FLUX – STATIC ENGINE

### *General Characteristics*

Mean heat flux signals are shown for each fuel and temperature in **Fig. 10**; those refer to the cylinder location which produced the maximum heat flux. This generally occurred around -20°, *i.e.* on the intake side of the cylinder's bore (refer to **Fig. 5**). Due to the nominal symmetry of the spray's development under static-engine conditions, the heat flux at the locations of maximum wall impingement on the intake and exhaust side of the cylinder should have been 'identical'; however, they were some differences, as will be discussed later. The default heat flux value under static conditions was zero due to the differential nature of the signal. It should be reminded that the polarity of the heat flux value indicated the direction of heat flow into or out of the sensor, *i.e.* negative heat flux corresponded to heat flow out of the sensor, while positive heat flux was produced due to heat flow into the sensor. The time domain throughout the results is given in equivalent °CA ATDC at 1500 RPM; 1 °CA corresponds to 0.111 ms. This was decided in order to encourage the reader to follow the results holistically and facilitate comparisons with signals presented later in the present paper under full-load motoring engine conditions (1.0 bar intake pressure), as well as with earlier publications on spray imaging under low-load motoring and firing engine conditions (0.5 bar intake pressure) [19, 20, 28, 29]. In **Fig. 10**, a starting point of 80° CA ATDC (in the intake stroke) was used, denoting the Start Of Injection (SOI). No heat flux was registered during fuel injection (80°–90° CA ATDC). At ~95° CA ATDC, a steep spike was observed (*i.e.* around 15° CA ASOI or, differently, 1.67 ms ASOI); this negative peak marked the timing of liquid arrival on the sensor's face; the signal then gradually returned to zero as the thermopile returned to thermal equilibrium. Considering an average timing of fuel arrival at the cylinder wall of ~15° CA ASOI (1.67 ms) and the initial injector opening delay of ~0.3 ms, the average straight line spray tip velocity over this period was estimated to be ~30–40 m/s on average. This is in good agreement with spray imaging work and Phase Doppler droplet sizing measurements obtained with the same injector [30]. Different fuels not only produced different peak levels of heat flux in **Fig. 10**, but also different signal profiles on return to the zero level. These were the two most important characteristics of the heat flux signal for liquid impingement diagnostics and are discussed in the following sections.

### *Signal Interpretation*

The heat flux signal produced by sprays at different locations and by different fuels required careful analysis. Differences in average droplet sizes during spray formation for gasoline, *iso*-octane and ethanol fuels, measured by Phase Doppler, were found typically in the range 10–15% for fuel temperatures 20–90 °C at 1.0 bar ambient pressure [21, 30]. Furthermore, given that previous imaging studies had showed small differences in spray tip penetrations and cone angles between all fuels under quiescent conditions of 1 bar [22, 23, 30], where less than 5–10 % differences were typically quantified for fuel temperatures up to 90 °C, the heat flux signal was first considered to be a measure of the temperature difference $\Delta T$, between the impinging fuel and the sensor. The differences observed in the heat flux of different fuels were therefore attributed to different physical properties of the fuels (boiling point, latent heat of evaporation, *etc.*) that governed the heat and mass transfer during evaporation of the spray's droplets on their flight from injector nozzle exit to wall impact.

Having the simulated wet-bulb temperature values as a reference for all fuels, tests were carried out to identify experimentally the average temperature of the liquid impinging on the sensor face. A fixed engine head temperature of 20 °C was used for all tests and only the liner temperature was varied between ~10 °C and ~90 °C for five or six temperatures, to acquire enough data points to draw a suitable 'calibration' curve. At one of these test combinations, the peak heat flux value approached zero and turned positive, indicating hotter impinging liquid relative to the sensor face temperature. **Fig. 11** shows the mean heat flux traces and the averaged peak heat flux values calculated from 100 injection events, *i.e.* not the peak of the mean heat flux trace (again with the polarity reversed to facilitate display). The vertical bars on the peak heat flux graphs show the absolute range of variability around the mean, calculated from the COV.

The sensor temperatures at which the 'zero heat flux' transition points occurred showed good agreement to the simulated liquid wet-bulb temperatures, as summarised in **Table 3**. In particular for the alcohol fuels, the agreement with the simulated values was very good, with ethanol showing the zero heat flux point at ~10 °C and butanol at ~20 °C. For *iso*-octane a value of ~6 °C was obtained by extrapolation close to the lowest temperature tested; this also agreed well with the simulations that predicted a value of 7 °C. For gasoline and E10, the wet-bulb temperatures were too low to approach experimentally with the current cooling arrangement, as sensor temperatures below 0 °C would be required for that; however, by extrapolation the values obtained were -7 °C and -3 °C respectively, *i.e.* still quite close to the wet bulb temperatures predicted by the model. The comparison was better for the multi-component fuels and *iso*-octane if one considered the temperatures predicted by the model at ~1.1 ms from the start of evaporation; these were ~1 °C higher than the predicted final wet-bulb temperatures. The timing of 1.1 ms corresponded to the duration of fuel flight from the injector nozzle to the point of impact on the heat flux sensor (after electronic driver delays had been subtracted, as discussed earlier).

These results suggested that the liquid droplets, had on average reached their steady state temperature by the time they impinged onto the sensor's face; this was an important finding in terms of interpretation of the heat flux signal as it confirmed that the value of peak heat flux recorded, accurately reflected the temperature differences between liquid media and sensor face. It also highlighted the need of accurate control of the sensor's temperature for good practice and accuracy. For example, one of the tests involving butanol at 20 °C shown in **Fig. 11** showed a slightly positive heat flux signal, suggesting that the liquid fuel was slightly hotter than the nominal 20 °C that it was injected at, or that the sensor was slightly cooler than the nominal experimental test point. The sensor temperature data acquired during the test were studied and the latter hypothesis was discarded. Therefore, the fuel temperature, controlled indirectly via the engine's head water cooling system, was likely a little over 20 °C during this test, as the water system controller duty cycle had a range of ±1.5 °C. Clearly when such variations occurred very close to the heat flux polarity transition temperature – remember that butanol at 20 °C was predicted to have a wet bulb temperature of 18 °C by the single droplet model *i.e.* very close to 20 °C – the small changes in liquid fuel temperature during the injection process highlighted the need for careful control of the relative temperatures of the system. These effects were not manifested in the measurements of the other fuels, as their wet-bulb temperatures were much lower than the test operating temperatures.

In **Fig. 11**, the temperature *vs.* peak heat flux relationship for *iso*-octane was almost linear. For the multi-component fuels, gasoline and E10, the trends where more similar to *iso*-octane's but there were slight deviations at lower temperatures, particularly for E10. Pure alcohols, however, showed highly non-linear behaviour. Those differences are believed to arise from effects related to the higher latent heat of evaporation of the alcohol fuels. The effects also appeared to be exaggerated at higher temperatures, when approaching the boiling points of the fuels, due to the rapid rate of evaporation of the liquid films. For ethanol, a noticeable change in gradient occurred at ~35 °C and for butanol at ~50–65 °C. Linear trendlines showed that E10 had the highest sensitivity at 1.87 W/cm$^2$/°C, *iso*-octane followed with 1.71 W/cm$^2$/°C, then gasoline with 1.55 W/cm$^2$/K, ethanol at 1.00 W/cm$^2$/°C and butanol at 0.5 W/cm$^2$/°C. The values for alcohols were calculated using the first three low temperature points to exclude the effects of evaporative cooling. If evaporative cooling was considered, by using trendlines made up from the three highest temperature points then ethanol would have a sensitivity of ~3.0 W/cm$^2$/°C and butanol ~2.5 W/cm$^2$/°C. This was an interesting result because the difference between the latent heats of these two alcohols was ~0.7 which approached the difference between the measured sensitivities. Analysis of heat flux signals at other spatial locations of lower levels of fuel impingement (as will be discussed later), showed a drop in peak heat flux too but the trends among different fuels in **Fig. 11** did not change; the lines were of lower gradient but they still crossed the same zero-heat flux point.

Based on the discussion above, differences in average peak heat flux value under quiescent conditions can be interpreted as a true measure of differences in average relative temperature of impinging droplets for different fuels at a fixed location. However, other features of the heat flux signal, such as the 'width' of the signal around the value of peak heat flux and the rate of return to 'zero' level were also dependent on other quantities such as the fuel's evaporation rate, the latent heat of evaporation and the mass impinged; these are discussed next.

*Fuel Type and Temperature Effects*

As the engine coolant temperature was increased simultaneously for the engine head and liner, the signal was affected for the different fuels through their different rates of evaporation (**Fig. 10**). For the single-component fuels, the effect of increasing fuel temperature was an increase in the absolute values of measured heat flux. Higher initial fuel temperatures increased the evaporation rate and therefore the rate of cooling, which raised the temperature difference, $\Delta T$, between the impinging liquid and the sensor (the sensor was always at the same temperature to the initial fuel temperature).

For *iso*-octane the signal increased in magnitude and in width as the fuel temperature increased from 20 °C to 50 °C and then 90 °C. This was a result of evaporative film cooling at high sensor temperatures which slowed down the return of the signal to the zero level. At 90 °C the signals generally recovered to zero levels after about 120° CA ATDC faster than the signals at colder set temperatures.

Of note is the obvious 'kink' in the recovery of the signal for ethanol which is believed to stem from ethanol's high latent heat of evaporation. Also the latent heat of ethanol, *e.g.* when compared to *iso*-octane's, by contributing higher levels of cooling reduces the fuel film evaporation rate so that the signal at 90 °C does not cross over the signal obtained at 50 °C, in contrast to what observed for *iso*-octane. The signals at 20 °C

recovered quickly back to zero for all fuels because of the lower levels of heat transfer involved and the low levels of evaporative cooling, which allowed thermal equilibrium to be reached quickly.

E10 produced the highest peak heat flux at 50 °C, followed by ethanol and gasoline, both producing very similar values, and finally *iso*-octane and butanol. The ethanol-based fuels were the slowest to return to equilibrium, followed by *iso*-octane and gasoline, whose signals overlapped, indicating very similar overall levels of heat transfer. Butanol produced more negative heat flux at 50 °C than at 20 °C, as expected from its predicted lower wet-bulb temperatures and the consequently higher $\Delta T$. At 90 °C the hierarchy of the heat flux changed once again. This time, ethanol and butanol produced the highest heat fluxes, followed by E10, *iso*-octane and gasoline. The widest signals were also produced by ethanol and *iso*-octane, while butanol was the slowest to return to equilibrium. A summary of the general trends observed with respect to the amplitude of peak heat flux for all fuels is given in **Table 4** for direct comparisons and clarity.

The combined results of the three temperature conditions allowed some decoupling of competing effects. It was clear that the wet-bulb temperature was not solely responsible for the differences observed when increasing the fuel temperature. Specifically, for gasoline and E10, the predicted wet-bulb temperatures for an initial liquid temperature of 90 °C were about 7 °C compared to 2 °C for 50 °C. Therefore, one might have expected lower heat fluxes at 50 °C, as a result of the lower $\Delta T$ between the impinging liquid and the sensor; however, this was not the case. Within this frame, the potential of lower levels of fuel mass impingement at 90 °C was considered. On the basis of the distillation curves of the multi-component fuels, 'flashing off' of the lighter components and subsequent changes in spray geometry (as observed for the same injector and fuels in [22, 30]) should have changed the amount of mass impinging on the sensor face at the same location in comparison to 50 °C. Specifically, the single droplet simulations for gasoline and E10 predicted that within the timescales taken for these fuels to reach the cylinder walls, a significant volume fraction had already evaporated. It is interesting to also note that at 90 °C there was a small but noticeable delay in the liquid arrival at the walls for both gasoline and E10 as shown by the late falling of the signal compared to 50 °C. This delay was likely due to the 'removal' of the spray's leading edge from rapid evaporation and improved spray plume break-up at such high temperatures [30]. The return signal at 90 °C was nearly identical for gasoline and E10, which was not the case at 50 °C. These results suggested that at 90° C the impinging liquid had lost a significant amount of its high volatility components, hence it did not contribute significant cooling at these temperatures, explaining the similarities between the two fuels. These similarities could be a balance of E10's slightly lower wet-bulb temperature but also lower direct liquid mass impingement from better break up and evaporation during spray development [25]. For pure ethanol and *iso*-octane the effects of evaporative cooling at 90 °C were greater and very clear from the wider return signal, while butanol was more similar to the multi-component fuels and evaporated slower.

*Sensor Location Sweeps – Peak Heat Flux*

The results presented so far highlighted that under typical conditions and with validated assumptions, *e.g.* that the liquid impinging on the sensor had generally reached its steady state wet-bulb temperature, that the mass levels were low enough and/or the sensor hot enough to avoid signal saturation or reduced sensitivity, then the peak heat flux itself could potentially be used as a measure of the mass of fuel impinged on the sensor when changing sampling locations around the cylinder bore, thus build a map of impingement along the

circumference of the cylinder's liner. In this context, the usefulness of the heat flux signals with regards to spray pattern characterisation becomes apparent when showing the peak heat fluxes in **Fig. 12** for a sweep of cylinder locations; the injection-to-injection variability of the peak heat flux is also displayed in the same figure in the form of COV. Please note that the mean peak heat flux values shown in **Fig. 12** are not necessarily identical to those shown in the average signals presented earlier in **Fig. 10** for the -20° location because the values in **Fig. 12** are averages of the injection-to-injection recorded peaks (irrespective of shot-to-shot variability in the timing of peaks), whilst the peak values in the traces of **Fig. 10** correspond to ensemble-averaged heat flux traces. In general, **Fig. 12** shows a relatively symmetrical bimodal distribution of wall heat flux as the sensor was swept past the two main impingement locations of spray plume #1 (left peak on the figure) and spray plume #6 (right peak on the figure); this is compatible with the liquid fuel impingement locations identified by spray imaging. The attentive reader will also notice that the locations of peak heat fluxes were not 'symmetrical' about the 0° location for any of the fuels or conditions in **Fig. 12**. The peaks for plume #1 generally occurred around -20° and for plume #6 around +30° or +35°. This might initially suggest a geometric asymmetry in the trajectories of the spray plumes, but in reality it was found to be a characteristic of the offset injector location within the engine head itself with respect to the cylinder's axis, as also can be seen in the image of **Fig. 5**. Furthermore, it was identified that the small differences in peak heat flux of the otherwise 'nominally same' spray plumes #1 and #6 were introduced by the presence of the asymmetric spark plug with single J-type ground electrode that the two plumes passed by in very close proximity on either sides that led to occasional asymmetric 'splashing' onto the electrode during spray formation (*e.g.* from transient spray 'flapping' behaviour; *e.g.* see [21] for a typical analysis). The effect was less pronounced at higher fuel temperatures.

The heat flux recorded between the locations of maximum heat flux was not a result of direct head-on spray plume impingement but primarily due to nearby direct impact and subsequent splashing/secondary atomisation; it is also believed that impact of airborne droplets originating from the plumes' breakup during spray development also contributed to the signal at these locations. This was also supported by studying the timing of impingement. At those locations of low heat flux, large values of COV were recorded; the largest values of COV were observed for *iso*-octane at 90 °C along with the lowest heat flux values. At other locations and temperatures, the COV was found to range between 20–40 % for most fuels and any deviations from this were signs of local fluid dynamic and transport property effects. Butanol's peak heat flux value at 20 °C was either very close to zero or slightly positive. Ethanol generally produced lower levels of COV than gasoline or *iso*-octane at 20 °C, which may have been an indicator of more repeatable spray formation, *e.g.* due to the lower degree of break-up and atomisation observed by spray imaging [30]. At 90 °C, *iso*-octane showed similar values of heat flux to those of gasoline, but the levels of COV were marginally lower for *iso*-octane. These trends were consistent at the lower temperatures as well, which also indicated a greater direct repeatability of spray formation and impingement for *iso*-octane than for gasoline. For E10 the COV trends were similar to gasoline's, even though peak values of heat flux for E10 were higher by ~25%, presumably due to the higher latent heat of evaporation from the 10% ethanol content.

For *iso*-octane, higher values of heat flux were obtained at 90 °C than at 50 °C. The locations of maximum impingement were narrower and more confined to the axis of the spray plumes (either side of -20° and +30°),

with effectively zero heat flux in-between (see locations of 0°–10° and also note the high levels of COV at these locations). For ethanol, when the temperature was increased from 50 °C to 90 °C, the recorded levels of heat flux almost doubled which illustrated greater effects from faster evaporation and cooling, as the sensor surface was hotter than the boiling point of ethanol. The strong effect of cooling was noticeable across all impingement locations; the areas around the periphery of main impingement (-20° and 35°) also showed considerable levels of heat flux compared to lower temperatures and the COV also remained low. These results suggest that careful consideration of the latent heat of evaporation is essential under such conditions because initial observations can be counterintuitive when trying to provide a realistic profile of liquid impingement by comparing fuels. Nevertheless, for a fixed fuel, measurements of heat flux at different engine head temperatures are indeed capable of revealing differences in the spray's geometric 'envelope' from changes in the mechanism of atomisation as the fuel temperature is changed.

*Sensor Location Sweeps – Timing of Peak Heat Flux*

The time elapsed from SOI to liquid fuel impingement on the sensor face was defined by the location of the peak heat flux signal. These results are shown for all fuels and temperatures in **Fig. 13**. For some test points where near zero heat flux was recorded (*e.g.* see *iso*-octane at 90 °C around the 0–10° locations in **Fig. 12**), there was effectively no real peak in the signal for the automated data processing routine to pick out and the value generated in these cases was automatically set in **Fig 13** to BDC. **Fig. 13** also includes information about the injection-to-injection repeatability of the timings of peak impingement in the form of COV. The latter was naturally lower at the locations of highest heat flux. Regions of lower heat flux had higher COV, illustrating the greater degree of variability in the dynamics of splashing and/or secondary atomisation which indirectly delivered fuel to these locations. Overall, the timing of impingement exhibited an inverted double dip distribution across the different sensor locations. This was more accentuated for ethanol than for *iso*-octane or gasoline, especially at 20 °C and 50 °C. The timings of impingement either side of the main impingement locations were greater for ethanol probably because these locations were mainly subject to secondary impingement from splashing events originating nearby. A similar trend was observed for butanol at 50 °C. By 90 °C however, the trends for the alcohols resembled more closely those of *iso*-octane and gasoline at 20 °C because the higher temperature improved the spray atomisation process. Overall **Fig. 13** shows that the timing of impingement was remarkably similar for all fuels in the short distance of flight from the injector tip to the cylinder wall. The high momentum of the injected sprays was such that impingement timings varied only by ±100 μs (or ~1° CA equivalent at 1500 RPM) for the main impingement locations. However, other locations that were affected indirectly by the main impingement dynamics and the break-up characteristics were more specific to each fuel type and produced more variable timings of liquid impingement.

SPRAY WALL IMPINGEMENT HEAT FLUX – MOTORING ENGINE

*General Characteristics*

The effect of in-cylinder flow on liquid fuel impingement heat flux was investigated by motoring the engine with wide-open throttle, *i.e.* with inlet plenum pressure of 1.0 bar, nominally same to that of the static engine tests. **Fig. 14** shows an image of *iso*-octane's in-cylinder spray at those conditions for direct comparison to the respective image of **Fig. 5** under static engine testing. The effect of the incoming flow through the intake valves on the nominal spray pattern is clear. The spray plumes on the right hand side of the bore in **Fig. 5** are

heavily affected by the incoming flow through the right intake valve. The effect is not as strong on the left hand side because the spray plumes on that side are at less acute angle and do not cut straight through the left intake valve flow (see also spray schematic of **Fig. 1**). **Fig. 15** shows the mean heat flux signal under engine motoring conditions with and without fuel injection (at the location of maximum impingement) for direct comparison. The mean heat flux signals obtained at the location of maximum impingement for the different fuels at 20 °C and 90 °C initial fuel temperatures are shown in **Fig. 16**. It became immediately obvious that the absolute levels of peak heat flux at engine running conditions were significantly reduced and, in terms of impingement locations, the sweeps in **Fig. 17** showed similar patterns for all fuels. Overall the strong intake flow valve 'jet' was found to result in the complete destruction of the spray momentum for plume #1 and significantly deflected plume #6 towards the exhaust side of the combustion chamber, as also seen in the spray image of **Fig. 14**. Nearly zero heat flux was recorded in the region -30° to +20° and a clear shift of impingement was towards the exhaust side locations of +50° to +90°; this trend was very similar for all fuels. Considering that the wet-bulb temperature was not really affected by the presence of the in-cylinder flow, these trends suggested that lower levels of liquid mass impingement were taking place under engine motoring conditions. The magnitude of the heat flux measured on either side of the location of maximum impingement was also higher under motoring conditions, indicating a wider spread of impingement locations on the cylinder liner. In contrast, for static conditions, the locations of heat flux were more concentrated around the plume axes, reflecting the compactness of the plumes and the clear geometric pattern of the multi-hole spray under these conditions. The high levels of cyclic variability in heat flux on the intake side however, indicated that there were cycles with some degree of impingement even at these intake locations, which could be explained by cyclic variations in the spray's impingement due to cyclic variations in the incoming flow. The flow field in the intake runner and inside the cylinder of a nominally identical engine to that of the current paper has been investigated by Particle Image Velocimetry (PIV) in [33–35], where the formation and development of the tumble flow in the engine was characterised. The measured cyclic variability in that flow on the intake stroke was also compatible with the cyclic variability in the wall impingement of the spray plumes imaged in the current engine [28, 29].

The first feature of interest on the heat flux signal of **Fig. 15** was observed at the beginning of the intake stroke: due to the slightly negative valve overlap used in this work, a small vacuum was recorded on the in-cylinder pressure signals before the opening of the intake valves (IVO) and this depression manifested itself as a small dip on the heat flux signal (heat drawn out of the sensor); however, the signal recovered quickly back to the zero level when the intake valves opened at ~30° CA ATDC. For the dry motoring case (*i.e.* no injection) in **Fig 15**, the heat flux signal during the intake stroke was mostly flat since the air was at the same temperature as the sensor, 20 °C. For the wet motoring case (*i.e.* with fuel injection) in **Fig. 15**, liquid impingement resulted in a negative signal at ~95° CA ATDC, which gradually returned to zero levels before intake valve closure (IVC) as the impinged fuel film evaporated from the sensor face.

The motoring engine conditions without fuel injection resulted in positive heat flux values early in the cycle, up to ~1 W/cm$^2$ soon after intake TDC. Under motoring engine conditions with fuel injection, the heat flux traces show characteristics from previous-cycle effects. The main feature from those was reflected in the lower heat flux levels immediately after intake valve opening ~60° CA ATDC when compared to dry motoring.

Specifically, due to prior-cycle impingement events and the lack of complete film evaporation, particularly at 20 °C, the incoming flow past the sensor resulted in some cooling which was not seen for motoring without fuel injection. The incoming flow past the sensor produced noticeable levels of negative heat flux from evaporative cooling, *e.g.* of the order of 2 W/cm$^2$ at 20 °C for *iso*-octane.

After IVC, compression raised the gas temperature in the cylinder and positive heat flux was recorded. Before the peak at TDC, the signal showed a slight dip which was caused by the piston's top covering the sensor during the last ¼ of the engine stroke; a low ring-pack piston was used to avoid the piston rings scrapping past the sensor, hence the effect was simply due to masking of the sensor face by the piston's extended top land. After TDC, the heat flux decreased rapidly and reached a minimum at the point where the piston uncovered the sensor face again, specifically at ~400° CA in **Fig. 15**. The signal was slightly negative at this stage presumably due to fast flows within the crevice space between the piston and the sensor, but once the sensor was fully uncovered the signal quickly returned to zero levels. For the fuel injected case, there was a temporary negative dip around 480° CA, which is believed to result from a thin fuel film remaining on the sensor face even after compression. In this context, the sudden flow past the sensor when the exhaust valves opened (EVO) led to evaporative cooling that produced this effect; this characteristic was never observed under motoring conditions without fuel injection. For all injection events on a cycle-by-cycle basis, sensor locations which produced large signals in the intake stroke also produced large negative heat fluxes in the exhaust stroke and this was further confirmation that the fuel film produced from impingement was not fully evaporated during the compression stroke despite the high in-cylinder temperatures achieved.

*Fuel Type and Temperature Effects*

After the main impingement event, the heat flux signals took longer to return to zero levels in **Fig. 16** than at static conditions in **Fig. 10** and exhibited secondary dips as a result of forced convection on the remaining liquid film, causing further evaporative cooling on the sensor's face. This trend was seen mainly at 90 °C and was similar for *iso*-octane, gasoline and E10; *iso*-octane exhibited the weakest effect due to its higher boiling point relative to the sensor's temperature and lower latent heat of evaporation. For ethanol at 20 °C there was a significant negative heat flux during the intake period between 30°–60° CA ATDC in **Fig. 16**. The impingement heat flux during injection was relatively small at 20 °C. However, this did not necessarily imply low levels of fuel mass impingement; *e.g.* the negative heat flux produced in the exhaust stroke demonstrated that this was the case. The effect was eliminated at 90 °C as prior-cycle effects from accumulated fuel on the sensor face essentially disappeared. Ethanol's impingement produced a larger peak heat flux than the other fuels but this was still only 35% of the value obtained for static engine conditions. At high temperature, ethanol showed no major secondary dips from cooling, probably because most of the fuel evaporated quickly upon impact as a result of ethanol's low boiling point (78 °C versus 90 °C sensor temperature). Consequently, heat flux during the exhaust stroke was not generally observed either.

For butanol fuelling, the heat flux signal response at motoring engine conditions was poor, presumably as a result of butanol's high viscosity/surface tension and low evaporation rate that ultimately created a thicker fuel film on the sensor face that survived more from cycle-to-cycle than that of the other fuels. This affected the compression heat flux signal significantly by 'damping' the heat transfer rate; it seems that the sensor was not able to capture the transient effects with the same resolution as that observed with the other fuels at 20 °C. In

the exhaust stroke, no heat flux was generated which, coupled to the absence of heat flux in the early intake period, may again indicate sensor sensitivity issues due to fuel accumulation. At 90 °C, heat flux levels generated by butanol during the injection event were better than 20 °C, but the smallest of all fuels primarily due to butanol's higher wet-bulb temperature. The compression heat flux at 90 °C also indicated much better signal response than at 20 °C.

The levels of COV in peak heat flux were very similar for or *iso*-octane, gasoline and E10, but lower for the alcohols presumably due to the higher repeatability of impingement for these fuels associated with their spray formation characteristics.

*Relevance to Mass*

Calculation of measures of fuel mass from the integrals of the static engine's heat flux signals (**Fig. 10**) using the latent and sensible heats led to values of the order 1% of the injected mass per plume. As the engine temperature was raised from 50 °C to 90 °C, the calculated fuel mass was typically reduced by about 10–20% depending on fuel. The trends are reasonable when considering that the impinged liquid fuel has been observed by imaging studies to be lower at higher temperature than at lower temperature due to enhanced atomisation effects. In this context, the trends in evaporated mass fraction predicted by the droplet evaporation model are also in agreement.

For motoring engine conditions, to calculate measures of fuel mass from the heat flux traces, the difference between the non-fuelled motoring and fuelled motoring signal has to be integrated from the timing of injection up to a point in the cycle where the values of heat flux on both signals are equal, *i.e.* at some point during the compression stroke. Based on analysis of the integral and peak heat flux, as well as boiling points, the estimated measure of fuel mass can be attributed either to lower fuel mass impinged on the sensor, *e.g.* when changing injection strategy for fixed fuel type and engine running conditions, or to lower temperature from more evaporated fuel mass during flight from the injector's nozzle to sensor's face, *e.g.* for fixed fuel type with different engine head temperatures. The methodology can also be applied over various parts of the signal individually for more detailed analysis. Within this context, the difference between the integral of the heat flux signal around the exhaust-valve-open timing (where evaporative cooling was typically observed) was used to estimate the fuel mass on the sensor by comparing the fuelled and non-fuelled engine motoring conditions; then this mass was used to derive a wall film thickness based on the sensor's known dimensions. Analysis of a series of cycles led to values of wall film thickness in the range 0.1–1.0 μm. This is in agreement with trends quoted in the literature using significantly more complex optical techniques [5–11, 36]. The methodology is currently taken into further study by more data and analysis that could strengthen the diagnostics, *e.g.* by simultaneous heat flux measurements of fuel impingement on both the liner (vertically installed sensor face) and piston's crown (horizontally installed sensor face) to decouple effects related to the nature of the spray's flow on the sensor.

## SUMMARY AND CONCLUSIONS

Heat flux sensors mounted flush on the cylinder walls of a DISI engine were used to investigate fuel spray impingement from a centrally mounted multi-hole injector. *Iso*-octane, ethanol, butanol, gasoline and E10 were tested over engine coolant temperatures 10–90 °C. Tests were initially done at static engine conditions (*i.e.* in

quiescent environment at 1 bar) to isolate fuel-type effects. Then the engine was run with inlet plenum pressure of 1 bar to couple the intake air-flow effects to the heat flux signals. Interpretation and analysis also involved tests with monodisperse fuel droplet impact on the heat flux sensor's face, as well as modelling of the evaporation process of single droplets of all fuels at relevant spray conditions. The main conclusions are:

- Simultaneous imaging and heat flux sampling of single *iso*-octane droplet impactions on the sensor's face demonstrated great sensitivity of the heat flux signal to transient fluid dynamics. Integration of the heat flux signal predicted the mass of the impinged droplets with good accuracy (<2%).
- For fixed engine head temperature at 20 °C and liner temperature varied in the range 10–90 °C, the relationship between peak heat flux and liner temperature was almost linear for *iso*-octane. For gasoline and E10, the trends where similar to those of *iso*-octane but there were slight deviations at lower temperatures, particularly for E10. Both pure alcohols showed highly non-linear behaviour due their latent heat of evaporation; the effects appeared stronger at higher temperatures approaching the boiling points of the fuels. The fuel temperature at impingement obtained from those data indicated that the spray droplets had reached steady-state evaporation and the values agreed well with the wet-bulb temperatures of the droplet model.
- As the engine coolant temperature was increased from 20 °C to 90 °C for both head and liner, the signals were affected by the boiling point of the fuels. For *iso*-octane the signal increased gradually in both magnitude and width, as a result of evaporative film cooling which slowed down the return of the signal to zero level.
- Ethanol exhibited a distinctively wide shape over its recovery to equilibrium at 90 °C, believed to stem from its high latent heat of evaporation. The higher levels of cooling also reduced the fuel film evaporation rate so that the signal at 90 °C did not cross over the signal at 50 °C, in contrast to what observed for *iso*-octane. E10 produced the highest (negative) peak heat flux at 50 °C, followed by ethanol, gasoline, *iso*-octane and butanol. Ethanol and E10 were the slowest to return to equilibrium, followed by *iso*-octane and gasoline.
- At 90 °C butanol produced almost as high negative peak heat flux as ethanol, followed by E10, *iso*-octane and gasoline. The return signal at 90 °C was similar for gasoline and E10, which was not the case at 50 °C. Butanol's return to equilibrium was similar to gasoline and E10 and not at all as wide as ethanol's, despite the similar peak.
- The pattern of spray impingement was characterised by sweeping the heat flux sensor system over 140° on the periphery of the cylinder's liner, from intake to exhaust. A bimodal pattern emerged from the symmetry of the injector's geometry. The locations of direct fuel impingement were wider and less confined to the axes of the spray plumes at higher temperatures. The COV in peak heat flux ranged from 20–40 % for most fuels; any deviations from this were signs of specific spray dynamics.
- The timing of peak heat flux at the location of maximum impingement led to an average spray velocity of ~40 m/s at 20 °C. The COV in the timing of peak heat flux was ~10% (or lower) for the main impact locations for most fuels, but increased to over 20% for locations in-between and was more specific to each fuel type.
- At engine running conditions, the absolute levels of peak heat flux at impingement were reduced. The intake flow deflected the spray towards the exhaust side of the cylinder, eliminating the bimodal distribution observed under static engine testing. The levels of heat flux on either side of the location of main impingement were higher than under static conditions, indicating a wider spread of impingement on the liner.

- The heat flux signals took longer to return to zero than in the static engine and also exhibited secondary dips from evaporative cooling on the sensor's face. This was observed mainly at 90 °C and was similar in nature for *iso*-octane, gasoline and E10; *iso*-octane exhibited the smallest effect due to its boiling point and lower latent heat. At 90 °C, ethanol showed no secondary dips from cooling, probably because most of the fuel on the sensor evaporated quickly soon after impact.
- With butanol fuelling at 20 °C, the heat flux signal response at engine running conditions was poor as a result of butanol's high wet-bulb temperature, as well as high viscosity/surface tension and low evaporation rate linked to the creation of a thicker film on the sensor face that survived longer than that of the other fuels. This affected the compression heat flux signal significantly by damping the heat transfer rate. At 90 °C, butanol's peak heat flux levels were higher than at 20 °C, but still the smallest of all fuels. The compression heat flux at 90 °C also indicated much better response than at 20 °C.
- At the end of expansion, the flow past the sensor when the exhaust valves opened typically led to negative heat flux that had not been observed under running conditions without fuel injection. On a cycle-by-cycle basis, locations which produced significant negative heat flux in the intake stroke produced negative heat flux at the beginning of the exhaust stroke too. This was an indication that the fuel film had not evaporated fully.
- Under static engine testing, mass values of the order 1% of the injected fuel mass per plume were calculated from integration of the heat flux signals, with reductions of 10–20% noted when the engine temperature was raised from 50 °C to 90 °C. Under motoring engine tests, analysis of the signals by integration around exhaust-valve-open timing led to values of film thickness in the range 0.1–1.0 μm.

**ACKNOWLEDGMENTS**

The authors would like to thank Dave Richardson and Steve Richardson at Jaguar Cars for technical and financial support.

**REFERENCES**

1. Servati, H.B., Yuen, W.W., "Deposition of Fuel Droplets in Horizontal Intake Manifolds and the Behaviour of Fuel Film Flow on Its Walls", SAE Paper 840239, 1984.
2. Bardon, M.F., Rao, V.K., and Gardiner, D.P., "Intake Manifold Fuel Film Transient Dynamics", SAE Paper 870569, 1987.
3. Stanton, D.W., Rutland, C., "Multi-Dimensional Modelling of Heat and Mass Transfer of Fuel Films Resulting from Impinging Sprays", SAE Paper 980132, 1998.
4. Moreira, A.L.N., Moita, A.S. and Panão, M.R., "Advances and Challenges in Explaining Fuel Spray Impingement: How Much of Single Droplet Impact Research Is Useful?", Progress in Energy and Combustion Science, Vol. 36, pp. 554–580, 2010.
5. Park, S. and Ghandhi, J.B., "Fuel Film Temperature and Thickness Measurements on the Piston Crown of a Direct-Injection Spark-Ignition Engine", SAE Paper 2005-01-0649, 2005.
6. Cho, H. and Min, K., "Measurement of Liquid Fuel Film Distribution on the Cylinder of a Spark-Ignition Engine using the Laser-Induced Fluorescence Technique", Measurement Science and Technology, Vol.14, pp. 975–982, 2003.

7. Habchi, C., Foucart, H. and Baritaud, T., “Influence of the Wall Temperature on the Mixture Preparation in DI Gasoline Engines”, Oil and Gas Science and Technology – Rev. IFP, Vol. 54, No.2, pp. 211–222, 1999.
8. Stevens, E. and Steeper, R., “Piston Wetting in an Optical DISI engine: Fuel Films, Pool Fires and Soot Generation”, SAE Paper 2001-01-1203, 2001.
9. Lindgren, R. and Denbratt, I., “Influence of Wall Properties on the Characteristics of a Gasoline Spray after Wall Impingement”, SAE Paper 2004-01-1951, 2004.
10. Lindgren, R. and Denbratt, I., “Modelling Gasoline Spray-Wall Interactions and Comparison to Experimental Data”, SAE Paper 2004-01-3003, 2004.
11. Drake, M.C., Fansler, T.D., Solomon, A.S. and Szekely, G.A., “Piston Fuel Films as a Source of Smoke and Hydrocarbon Emissions from a Wall-Controlled Spark Ignited Direct-Injected Engine”, SAE 2003-01-0547, 2003.
12. Camacho, A. and Hall, M., “A Piezoelectric Sensor Concept for Measuring Piston Wetting in DISI Engines”, SAE Paper 2005-01-3873, 2005.
13. Shayler, P.J., Colechin, M.J.F. and Scarisbrick, A., “Heat Transfer Measurements in the Intake Port of a Spark Ignition Engine”, SAE Paper 960273, 1996.
14. Shayler, P.J., Colechin, M.J.F. and Scarisbrick, A., “Fuel Film Evaporation and Heat Transfer in the Intake Port of an SI Engine”, SAE Paper 961120, 1996.
15. Shayler, P.J., Colechin, M.J.F. and Scarisbrick, A., “Intra-Cycle Resolution of Heat Transfer to Fuel in the Intake Port of an SI Engine”, SAE Paper 960342, 1996.
16. Bauer, W., Balun, P. and Heywood, J.B., “Heat Transfer and Mixture Vaporisation in the Intake Port of a Spark-Ignition Engine”, SAE Paper 972983, 1997.
17. Balabin, R.M., Syunyaev, R.Z. and Karpov, S.A., “Quantitative Measurement of Ethanol Distribution over Fractions of Ethanol-Gasoline Fuel”, Energy and Fuels, Vol. 21, pp. 2460–2465, 2007.
18. Kar, K., Last, T., Haywood, C. and Raine, R.R., “Measurement of Vapour Pressures and Enthalpies of Vaporisation of Gasoline and Ethanol Blends and their Effects on Mixture Preparation in an SI Engine”, SAE Paper 2008-01-0317, 2008.
19. Serras-Pereira, J., Aleiferis, P.G., Richardson, D. and Wallace, S., “Mixture Formation and Combustion Variability in a Spray-Guided DISI Engine”, SAE Transactions, Journal of Engines, Vol. 116, No. 3, 1332–1356, SAE Paper 2007-01-4033, 2007.
20. Serras-Pereira, J., Aleiferis, P.G., Richardson, D. and Wallace, S., “Characteristics of Ethanol, Butanol, *iso*-Octane and Gasoline Sprays and Combustion from a Multi-Hole Injector in a DISI Engine”, SAE International Journal of Fuels and Lubricants, Vol. 1, pp. 893–909, SAE Paper 2008-01-1591, 2008.
21. Aleiferis, P.G., Serras-Pereira, J., van Romunde, Z., Caine, J. and Wirth, M., “Mechanisms of Spray Formation and Combustion from a Multi-Hole Injector with E85 and Gasoline”, Combustion and Flame, Vol. 157, pp. 735–756, 2010.
22. van Romunde, Z., Aleiferis, P.G., Cracknell, R.F. and Walmsley, H.L., “Effect of Fuel Properties on Spray Development from a Multi-Hole DISI Engine Injector”, SAE Transactions, Journal of Engines, Vol. 116, No. 3, pp. 1313–1331, SAE Paper 2007-01-4032, 2007.

23. van Romunde, Z. and Aleiferis, P.G., “Effect of Operating Conditions and Fuel Volatility on Development and Variability of Sprays from Gasoline Direct-Injection Multi-Hole Injectors” Atomization and Sprays, Vol. 19, pp. 207–234, 2009.
24. Serras-Pereira, J., van Romunde, Z., Aleiferis, P. G., Richardson, D., Wallace, S., Cracknell, R. F., “Cavitation, Primary Break-up and Flash boiling of Gasoline, *iso*-Octane and *n*-Pentane with a Real-size Optical Direct-Injection Nozzle”, Fuel, Vol. 89, pp. 2592–2607, 2010.
25. Aleiferis, P.G., Serras-Pereira, J., Augoye, A., Davies, T.J., Cracknell, R.F. and Richardson, D., “Effect of Fuel Temperature on In-Nozzle Cavitation and Spray Formation of Liquid Hydrocarbons and Alcohols from a Real-Size Optical Injector for Direct-Injection Spark-Ignition Engines”, International Journal of Heat and Mass Transfer, Vol. 53, pp. 4588–4606, 2010.
26. Butcher, A.J., Aleiferis, P.G. and Richardson, D., “Development of a Real-Size Optical Injector Nozzle for Studies of Cavitation, Spray Formation and Flash Boiling at Conditions Relevant to Direct-Injection Spark-Ignition Engines”, International Journal of Engine Research, in print, 2013.
27. Vatell Corporation, HFM-7, Heat Flux Sensor Documentation and Manuals, 2004.
28. Aleiferis, P.G., Serras-Pereira, J. and Richardson, D., “Imaging and Heat Flux Measurements of Impinging Sprays of Liquid Hydrocarbons and Alcohols in a Direct-Injection Spark-Ignition Engine”, Fuel, Vol. 91, pp. 264–297, 2011.
29. Serras-Pereira, J., Aleiferis, P.G., Richardson, D., Wallace, S., “Spray Development, Flow Interactions and Wall Impingement in a Direct-Injection Spark-Ignition Engine”, SAE Congress Brazil, November 2007, Sao Paulo, Brazil, SAE Paper 2007-01-2712, 2007.
30. Aleiferis, P. G. and van Romunde, Z., “An Analysis of Spray Development with Ethanol, Butanol, *iso*-Octane, *n*-Pentane and Gasoline Fuels from a Multi-Hole Injector under Hot Fuel Conditions”, Fuel, Vol. 105, pp. 143–168, 2013.
31. Faeth, G.M., “Current Status of Droplet and Liquid Combustion”, Progress in Energy and Combustion Science, Vol. 3, pp. 191–224, 1977.
32. Sirignano, W.A., “Fluid Dynamics and Transport of Droplets and Sprays”, CUP, 1998.
33. Justham, T., Jarvis, S., Clarke, A., Garner, C.P., Hargrave, G.K. and Richardson, D., “Single Cylinder Motored SI IC Engine Intake Runner Flow Measurement Using Time Resolved Digital Particle Image Velocimetry”, SAE Paper No 2006-01-1043, 2006.
34. Jarvis, S., Justham, T., Clarke, A., Garner, C.P., Hargrave, G.K. and Richardson, D., “Motored SI IC Engine In-Cylinder Flow Field Measurement Using Time Resolved Digital PIV for Characterisation of Cyclic Variation”, SAE Paper 2006-01-1044, 2006.
35. Justham, T., Jarvis, S., Clarke, A., Garner, C.P., Hargrave, G.K. and Halliwell, N.A., “Simultaneous Study of Intake and In-Cylinder IC Engine Flow Fields to Provide an Insight into Intake Induced Cyclic Variations”, Journal of Physics: Conference Series 45, pp.146-153, 2006.
36. Alger, T., Huang, Y., Hall, M. and Mathews, R.D., “Liquid Film Evaporation off the Piston of a Direct Injection gasoline Engine”, SAE Paper 2001-01-1204, 2001.
37. Scharlab S.L., Data Sheet 1-Butanol, HPLC grade, 2011.
38. Scharlab S.L., Data Sheet 2,2,4-Trimethylpentane, anhydrous, 2011.

39. Scharlab S.L., Data Sheet Ethanol absolute, analytical grade, ACS, 2011.
40. Shell Global Solutions (UK), Personal Communication, 2005.
41. Poling, B.E., Prausnitz, J.M. and O'Connell, J.P., "The Properties of Gases and Liquids", 5th Edition, McGraw-Hill, 2001.
42. Owen, K. and Coley, T., "Automotive Fuels Reference Book", Society of Automotive Engineers, 1995.
43. Yaws, C.L., "Yaws' Handbook of Thermodynamic and Physical Properties of Chemical Compounds", Knovel, 2003.
44. Gupta, R.B. and Demirbas, A., "Gasoline, Diesel and Ethanol Biofuels from Grasses and Plants", Cambridge University Press, 2010.

## LIST OF FIGURES



## LIST OF TABLES

**Table 1.** Fuel Properties [(a)].

| Properties | Ethanol | Butanol | Gasoline | *iso*-Octane |
|---|---|---|---|---|
| Chemical formula | $C_2H_5OH$ | $C_4H_9OH$ | $C_{6.75}H_{12.99}$ ($C_4$–$C_{12}$) | $C_8H_{18}$ |
| Molar mass [g/mol] | 46.07 | 74.12 | 100–105 | 114.3 |
| Density [g/cm$^3$] | 0.79 | 0.81 | 0.72 | 0.69 |
| Solubility in water (20 °C) [g/l] | miscible | 79 | partially | $5.6\times10^{-4}$ |
| Boiling point [°C] | 78.3 | 117.8 | ~55–145 (10–90%) | 99 |
| Flash point [°C] | 12 | 30 | -43 | -12 |
| Reid vapour pressure [kPa] | 16.1 [(b)] | 2.2 [(b)] | 56 | 11.8 [(b)] |
| Dynamic viscosity (20 °C) [cP] | 1.2 | 2.95 | 0.37–0.44 [(c)] | 0.51 |
| Dynamic viscosity (80 °C) [cP] | 0.43 [(d)] | 0.73 [(d)] | – | 0.27 [(d)] |
| Kinematic viscosity (25 °C) [cSt] | 1.34 [(d)] | 3.22 [(d)] | 0.5–0.58 | 0.67 [(d)] |
| Kinematic viscosity (80 °C) [cSt] | 0.59 [(d)] | 0.96 [(d)] | – | 0.42 [(d)] |
| Surface tension (20 °C) [mN/m] | 24.05 [(d)] | 26.3 [(d)] | ~20 | 18.3 [(d)] |
| Surface tension (80 °C) [mN/m] | 16.4 [(d)] | 19.3 [(d)] | – | 13.6 [(d)] |
| Latent heat ($T_{boil}$) [kJ/kg] | 855 [(d)] | 584 [(d)] | 364 | 272 [(d)] |
| Latent heat (25 °C) [kJ/kg] | 874 [(d)] | 669 [(d)] | 380–500 | 300 [(d)] |
| Specific heat capacity [kJ/kg] | 2.26 [(d)] | 2.76 [(d)] | 2.22 [(c)] | 2.03 [(d)] |
| Stoichiometric AFR | 9 | 11.1 | 14.6 | 15.1 |
| Heating value [MJ/kg], [MJ/lt] | 26.9, 21.3 [(d)] | 33.9, 27.5 [(d)] | 42.7, 32 [(c)] | 44.6, 30.8 [(d)] |
| RON | 129 [(e)] | 96 [(e)] | 95 | 100 |
| H/C | 3 | 2.5 | 1.92 | 2.25 |
| O/C | 0.5 | 0.25 | 0 | 0 |

(a) If not specified differently, data taken from product sheets [37–40]; (b) calculated from Poling *et al.* [41]; (c) calculated from Owen and Coley [42]; (d) calculated from Yaws [43]; (e) cited from Gupta and Demirbas [44].

**Table 2.** Heat Flux Sensor Specifications.

| Parameters | HFM-7 E/H |
|---|---|
| Maximum face temperature [°C] | 700 |
| Uncoated response time [μs] | 17 |
| Minimum HFM sensitivity [μV/W/cm²] | 150 |
| HFM impedance [kΩ] | 3.5 |
| Thermopile | Nichrome/Constantan |
| Temperature sensor | Platinum RTD |
| Temperature sensor sensitivity [°C/Ω] | 0.25–0.35 |
| Temperature sensor resistance [Ω] | 100–200 |
| Housing | Nickel |

**Table 3.** Wet Bulb Temperatures.

| Fuel | Wet Bulb Temperature [°C] | |
|---|---|---|
| | 1.0 bar, 20° C Model | 1.0 bar, 20° C Static Engine |
| *iso*-Octane | 7 | 8 |
| Gasoline | -6 | -7 |
| E10 | -5 | -3 |
| Butanol | 18 | 20 |
| Ethanol | 7 | 10 |

**Table 4.** Ranking of Absolute Mean Peak Heat Flux ($1^{st}$ = highest).

| Fuel | 20 °C | 50 °C | 90 °C |
|---|---|---|---|
| *iso*-Octane | $3^{rd}$ | $4^{th}$ | $4^{th}$ |
| Gasoline | $1^{st}$ | $3^{rd}$ | $5^{th}$ |
| E10 | $2^{nd}$ | $1^{st}$ | $3^{rd}$ |
| Butanol | $5^{th}$ | $5^{th}$ | $2^{nd}$ |
| Ethanol | $4^{th}$ | $2^{nd}$ | $1^{st}$ |

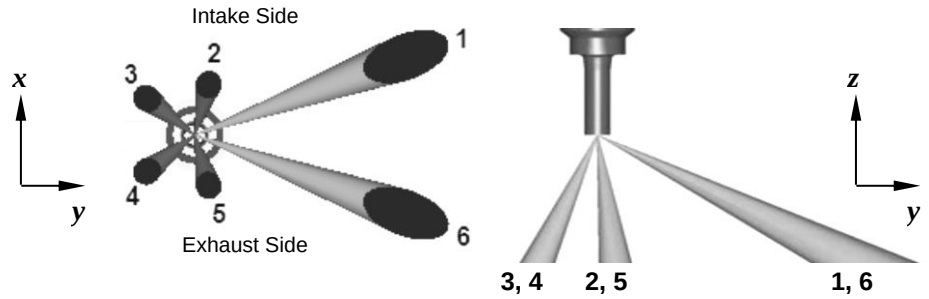


(a) (b)

**Fig. 1.** Schematic of Injector and Spray Plumes: (a) Piston View, (b) Exhaust Side View.

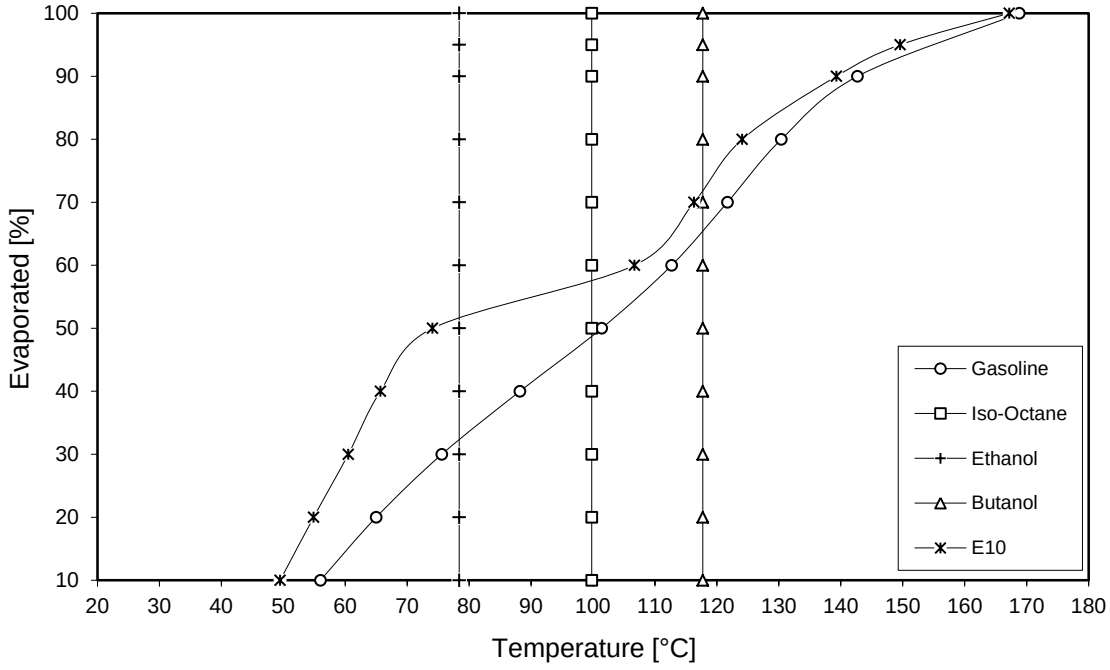


**Fig. 2.** Distillation Curves and Boling Points of Fuels Tested.

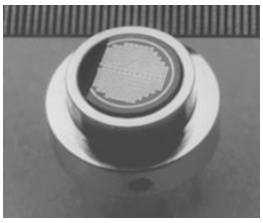

**Fig. 3.** Heat Flux Sensor [26].

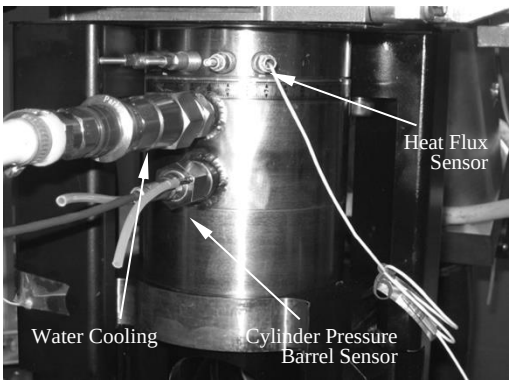


**Fig. 4.** Ring and Heat Flux Sensors Installed on the Engine.

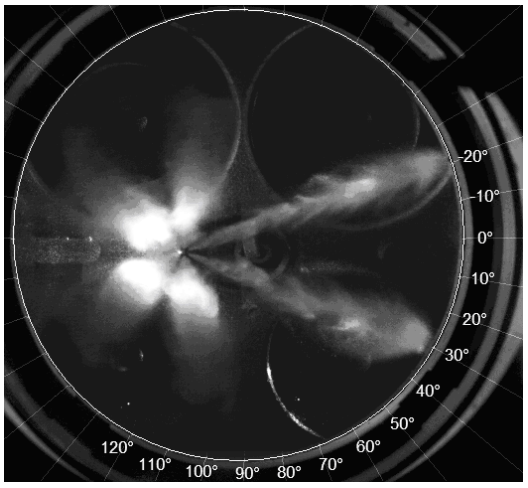


**Fig. 5.** Spray Image in Static Engine Overlaid with Polar Schematic of Sampled Heat Flux Locations around Cylinder Liner (*iso*-Octane, 20 °C, 10° CA ASOI; intake valves: top, exhaust valves: bottom).

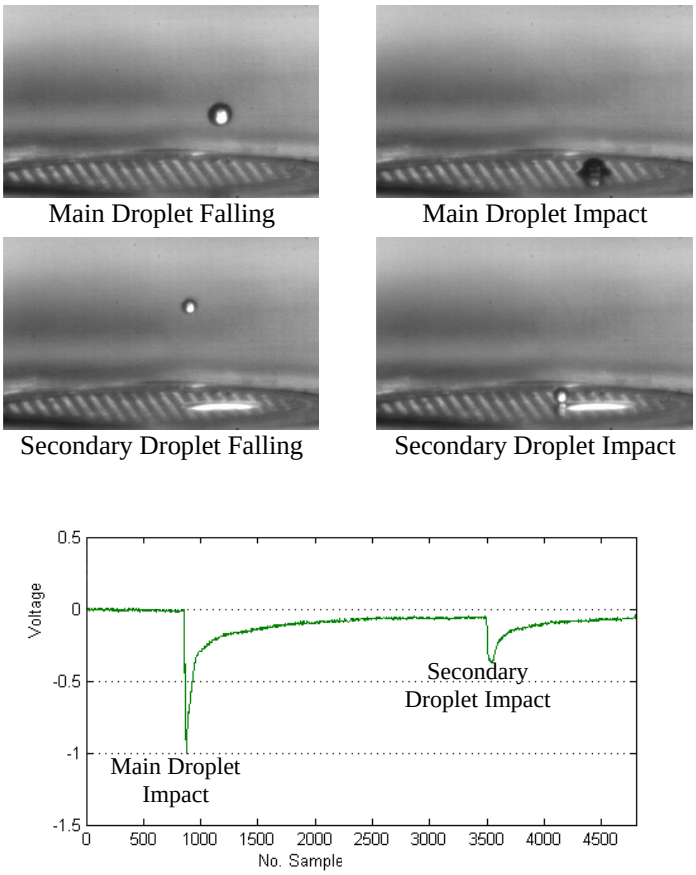


**Fig. 6**. Imaging of Single Droplet Impact on Heat Flux Sensor, Showing also Secondary Droplet Impact; Simultaneous Signal from Heat Flux Sensor (1 sample = 16.67 μs).

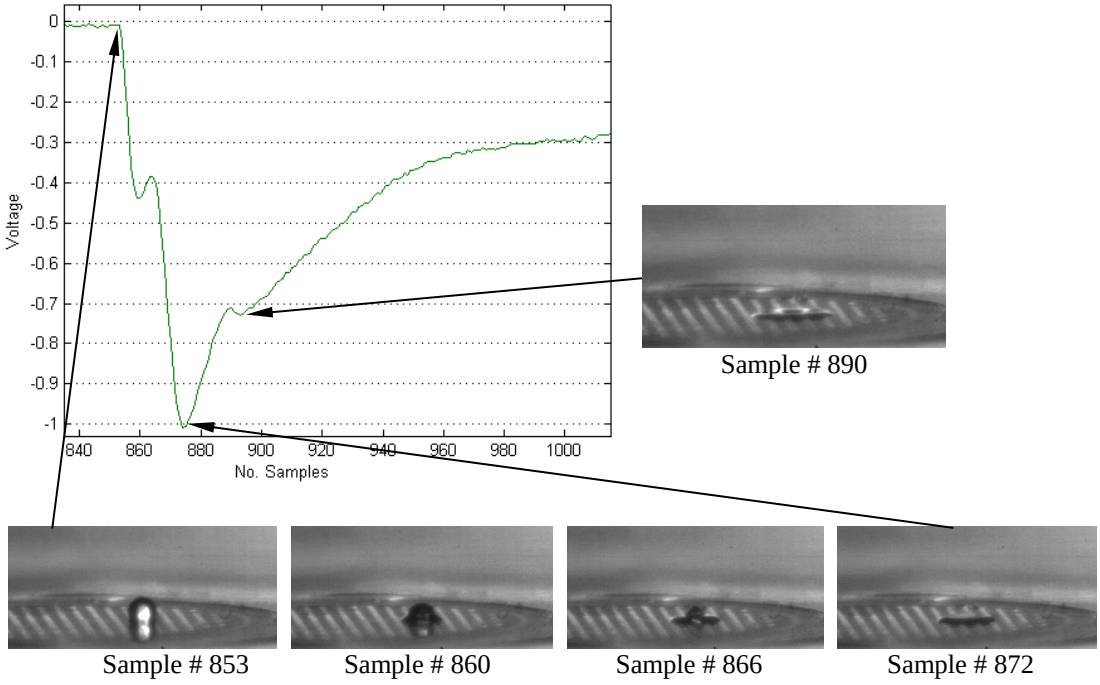


**Fig. 7.** Single Droplet Impact Dynamics and Simultaneous Heat Flux Signal (1 sample = 16.67 μs).

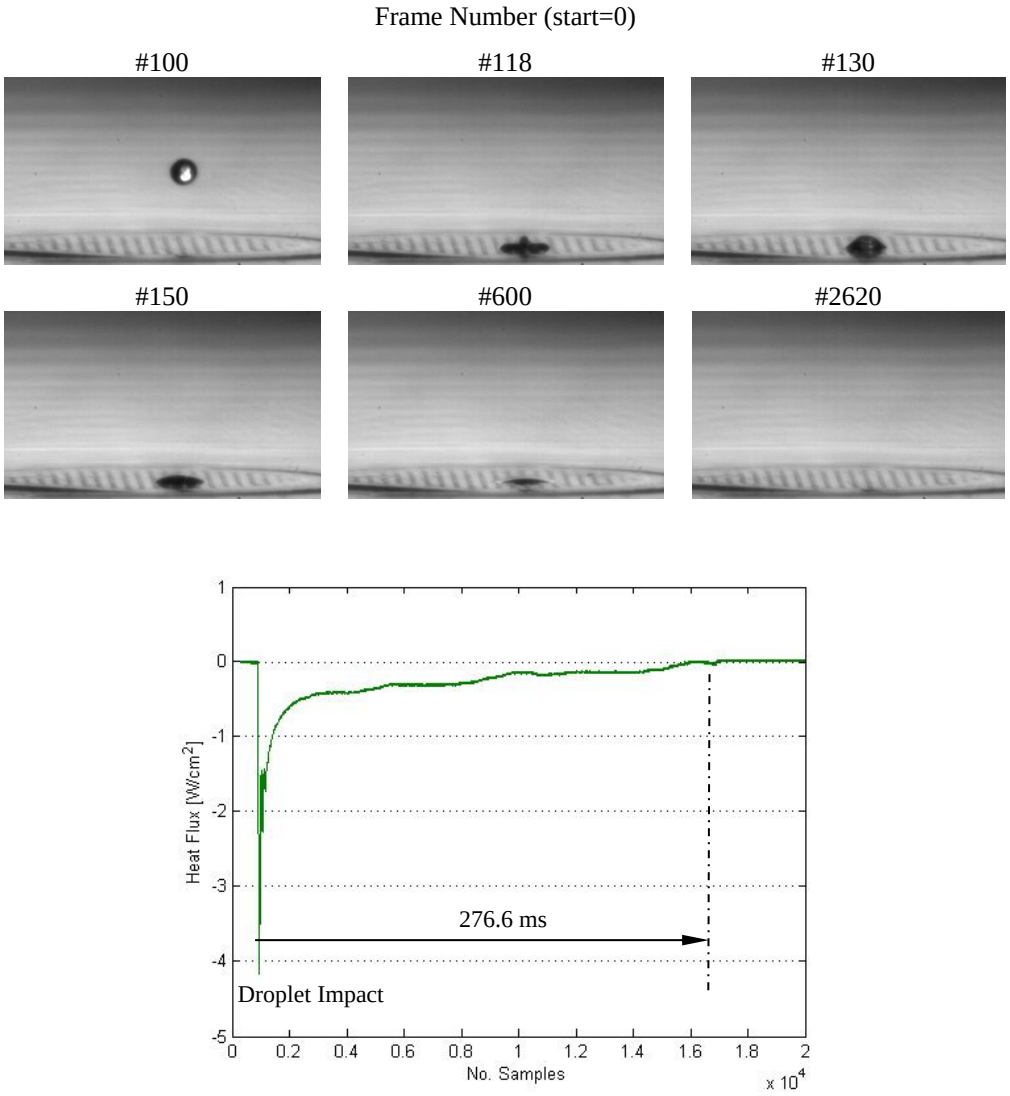


**Fig. 8.** Single Droplet Impact and Evaporation on Heat Flux Sensor (1 sample = 16.67 μs).

*iso*-Octane

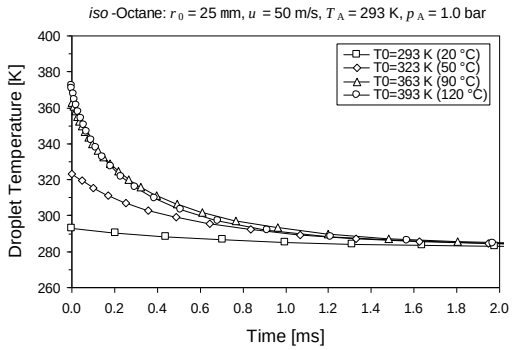


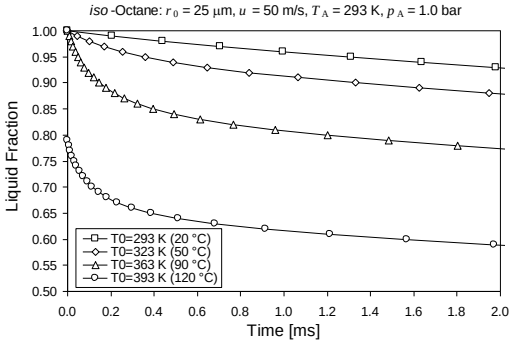


Gasoline

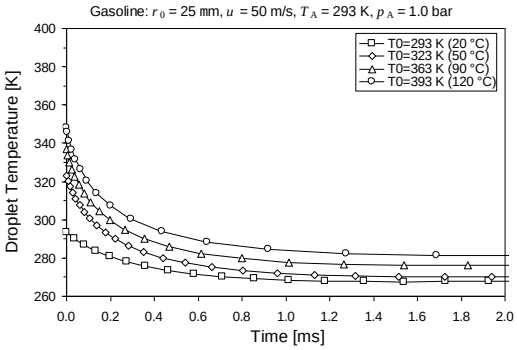


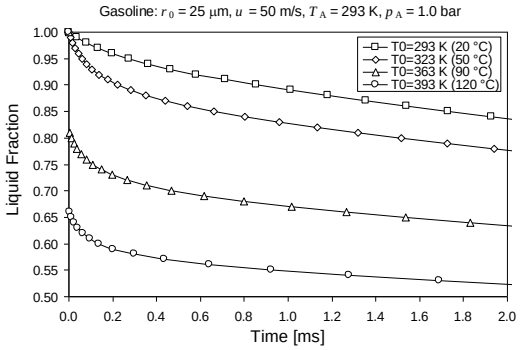


E10

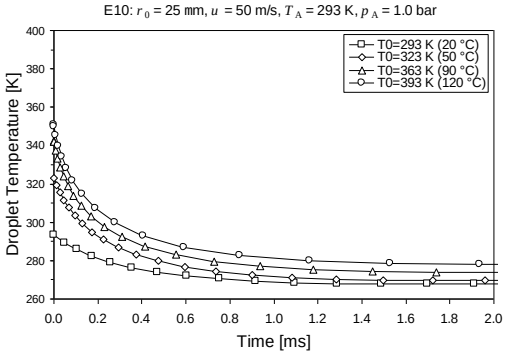


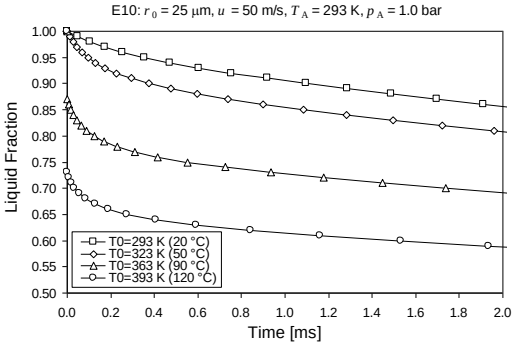


Ethanol

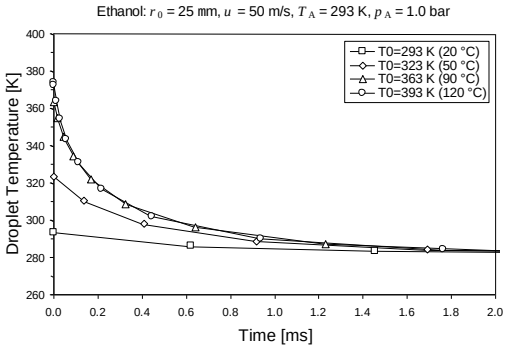


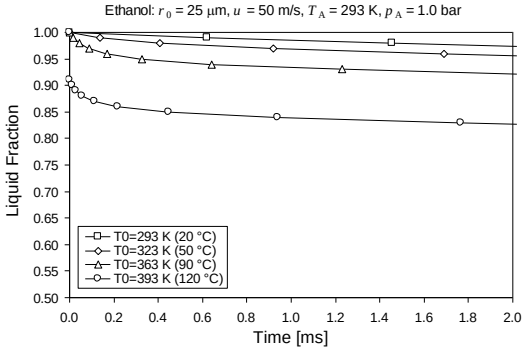


Butanol

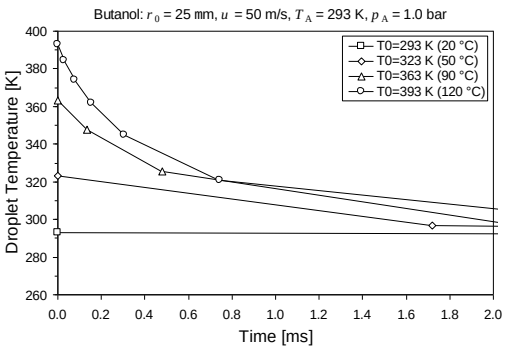


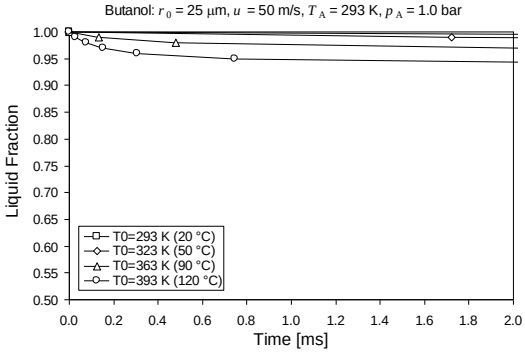


**Fig. 9.** Single Droplet Evaporation Results.

*iso*-Octane

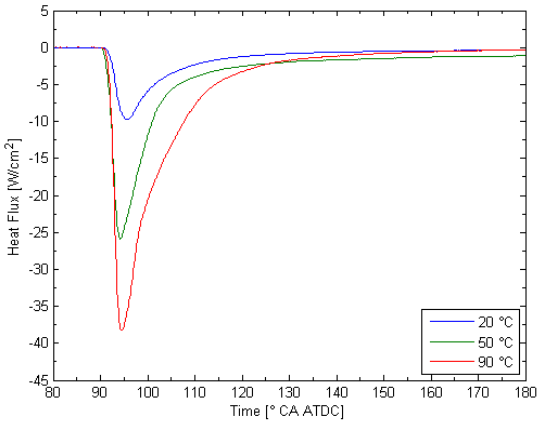


Gasoline

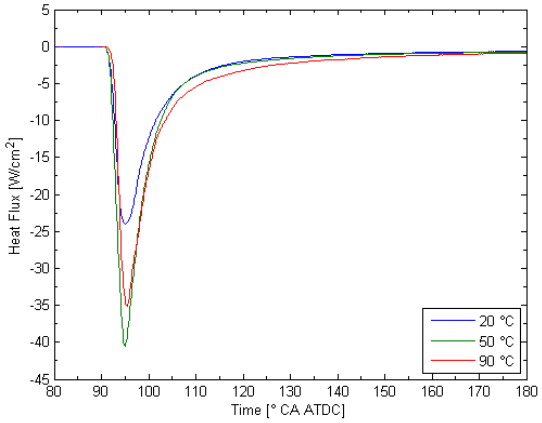


E10

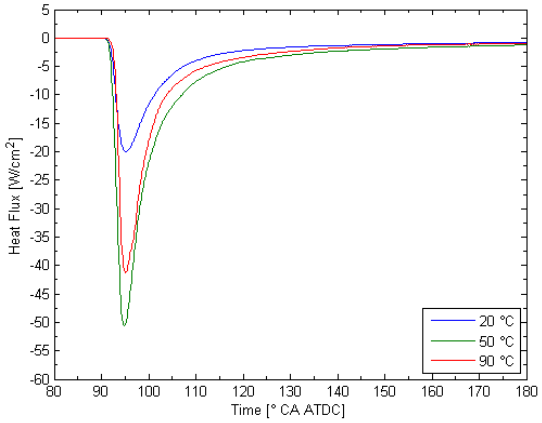


Ethanol

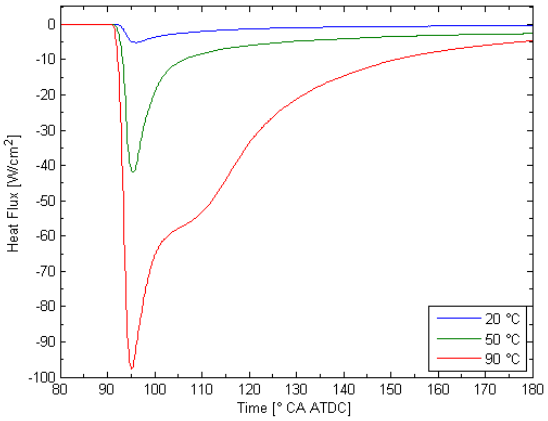


Butanol

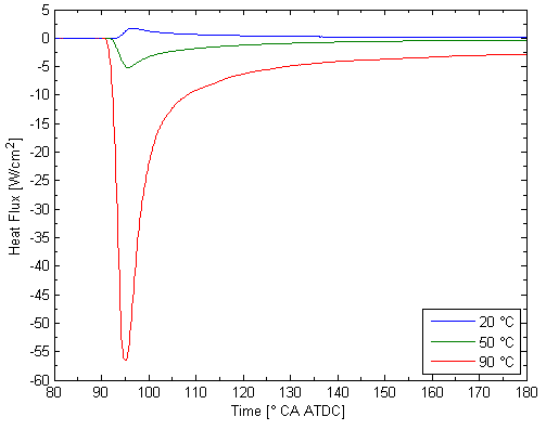


**Fig. 10.** Mean Heat Flux Signals with Different Fuel Types and Temperatures.

*iso*-Octane

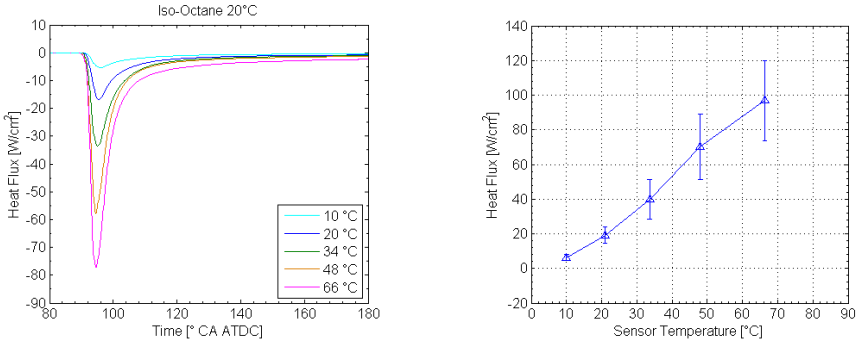


Gasoline

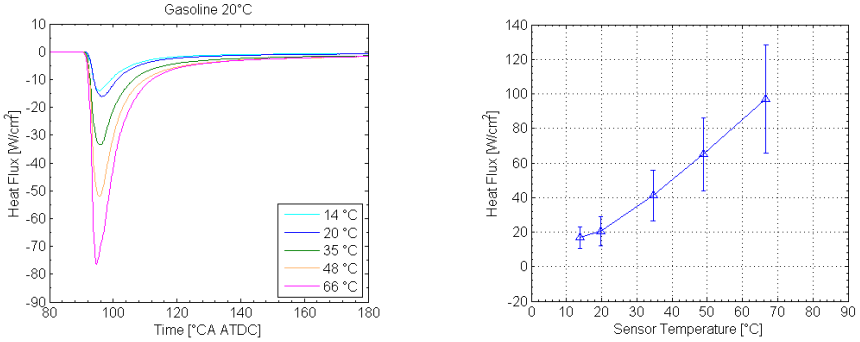


E10

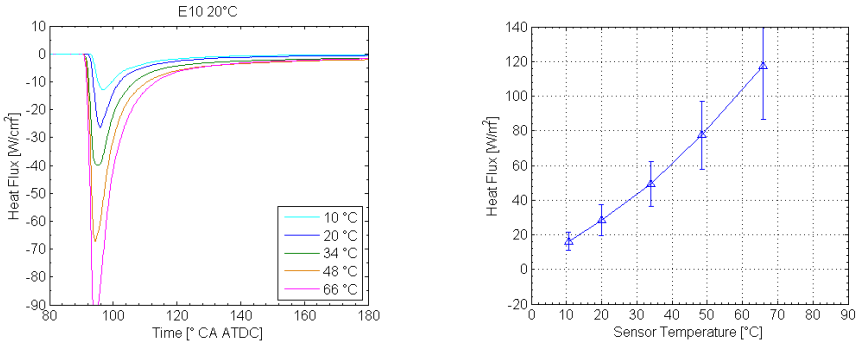


Ethanol

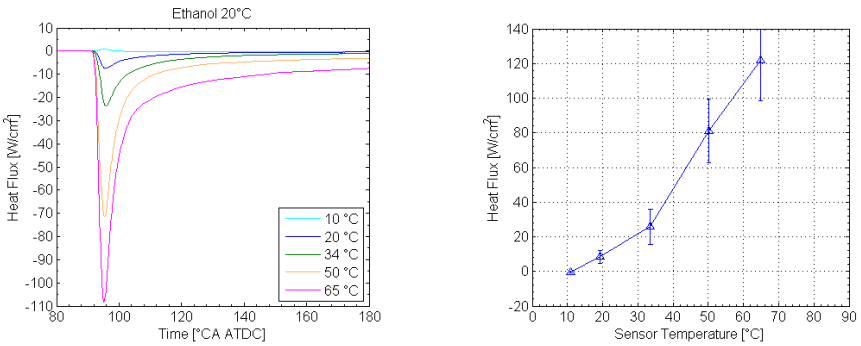


Butanol

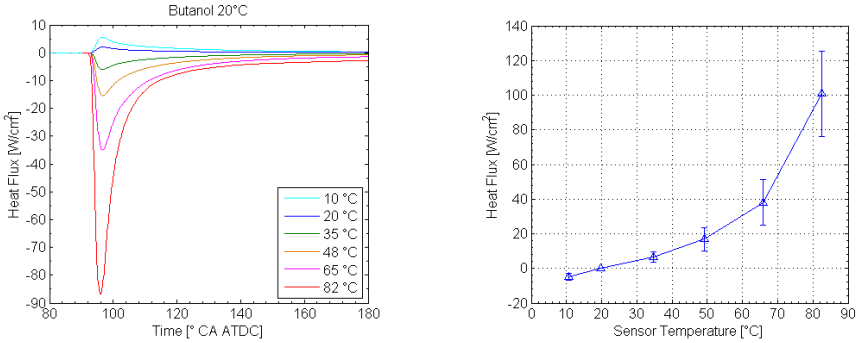


**Fig. 11.** Heat Flux Sensor Sensitivity and Determination of Liquid Impact Temperature: Mean Signals (left), Averaged Peak Values (right); Engine Head Temperature 20 °C.

*iso*-Octane

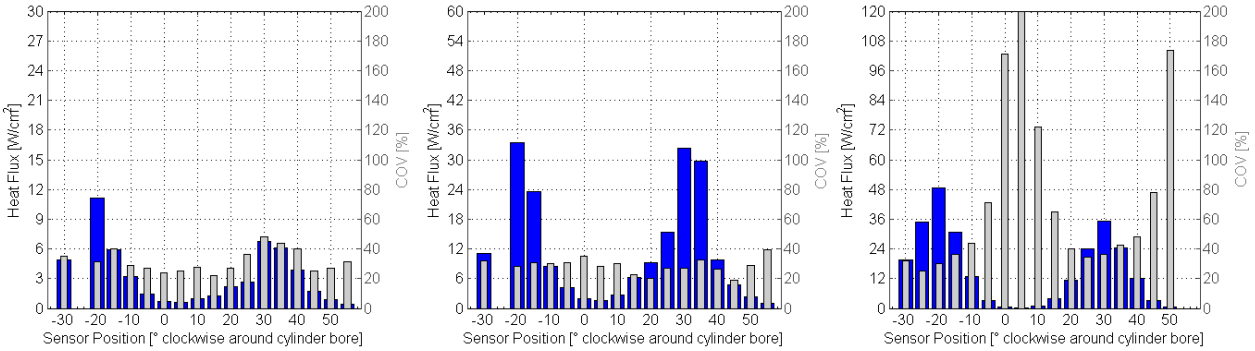


Gasoline

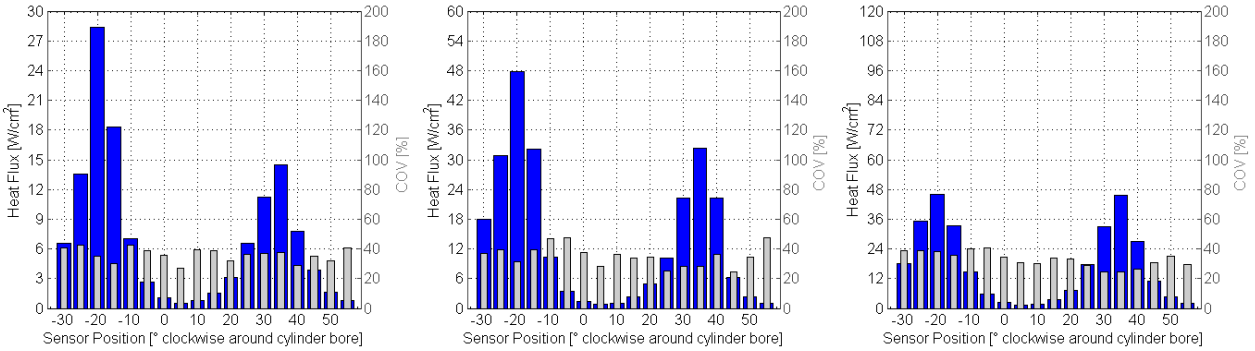


E10

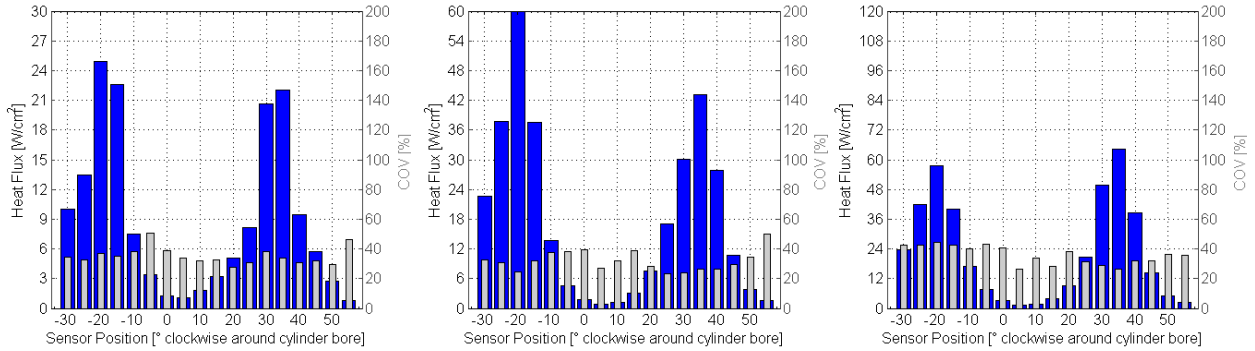


Ethanol

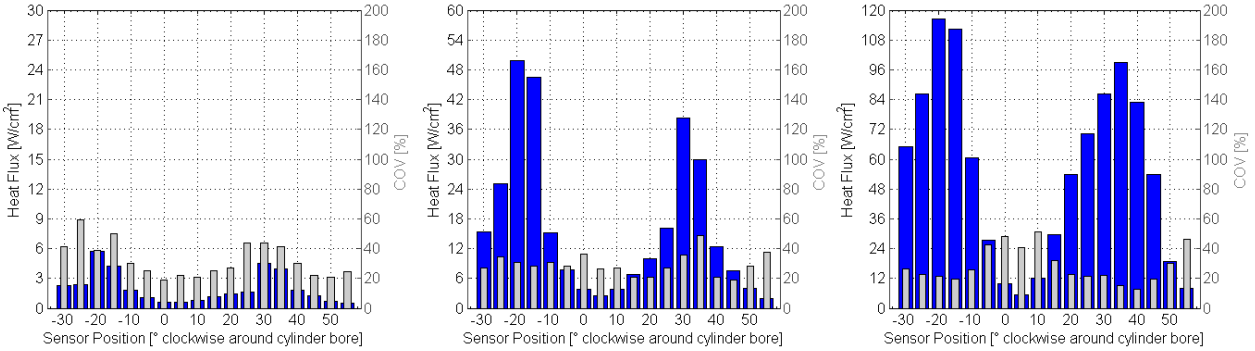


Butanol

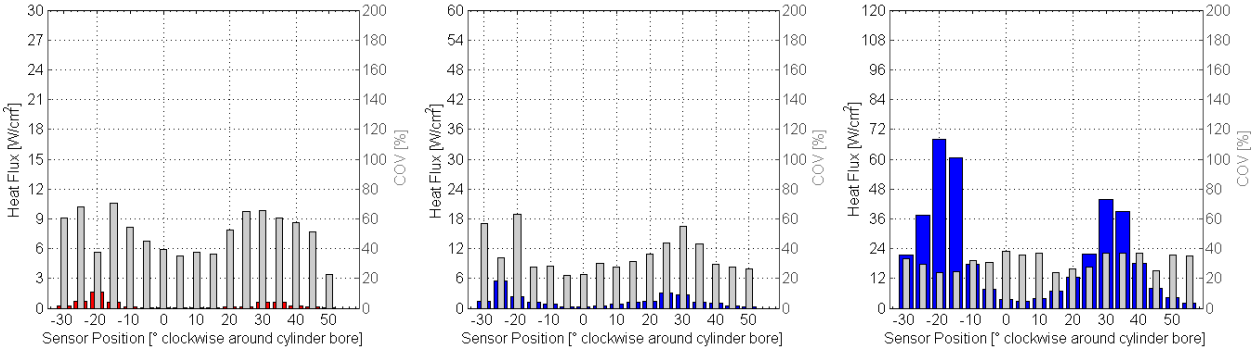


**Fig. 12.** Peak Heat Flux at Various Peripheral Locations for 20 °C, 50 °C and 90 °C (left to right); averaged values in colour, COV in grey.

*iso*-Octane

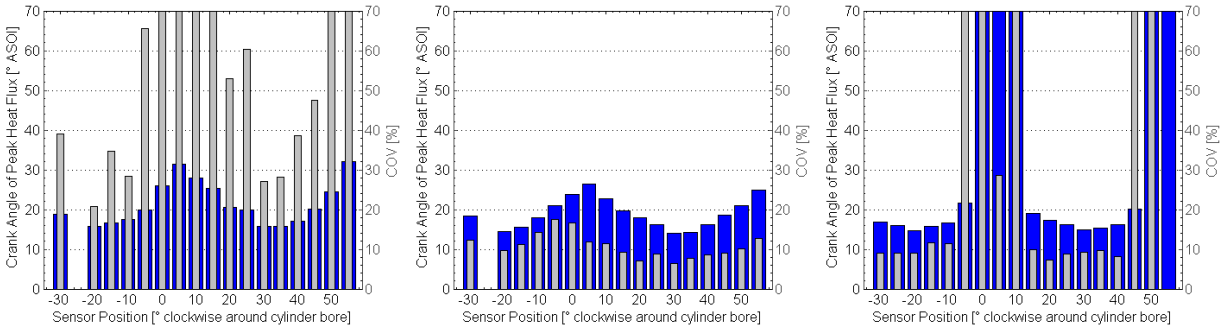


Gasoline

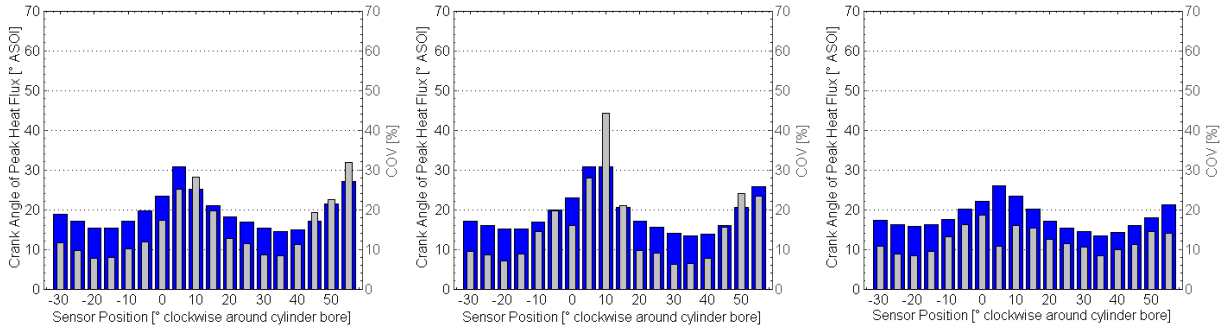


E10

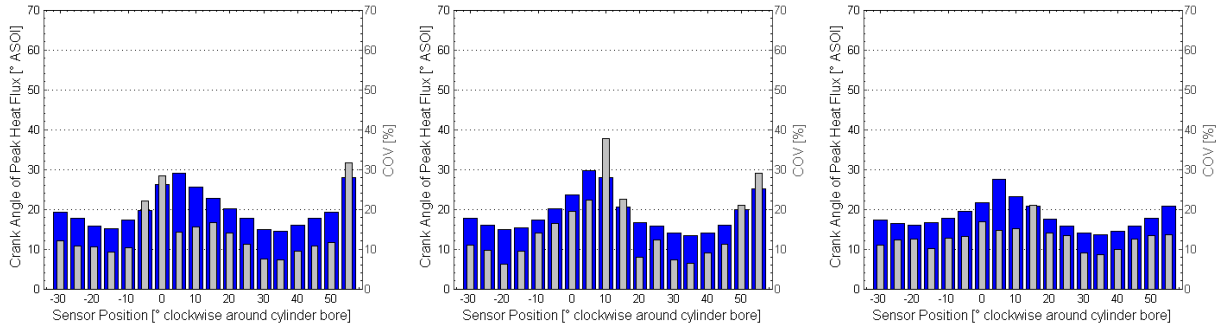


Ethanol

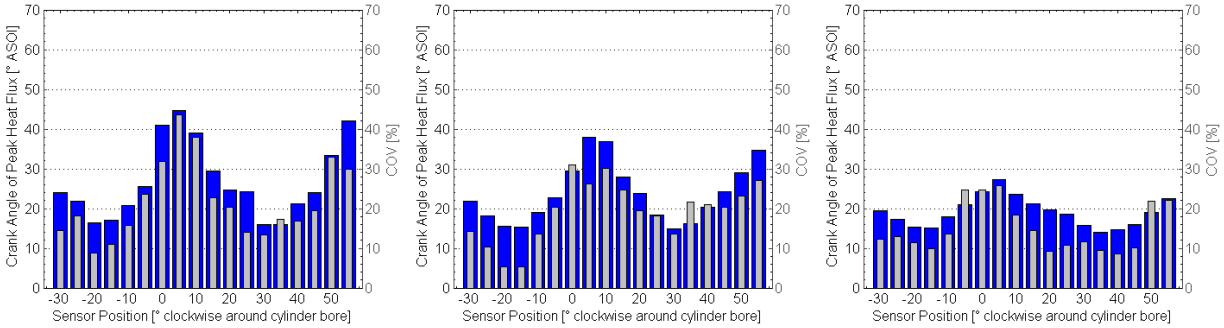


Butanol

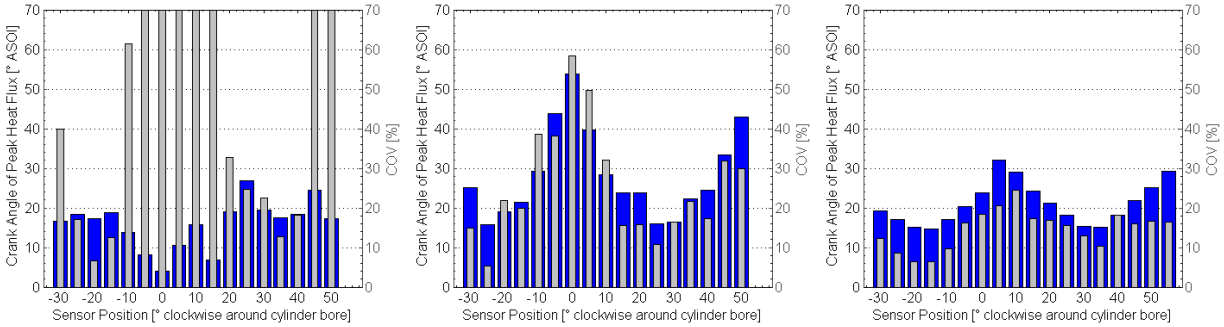


**Fig. 13.** Timing of Liquid Impact at Various Peripheral Locations for 20 °C, 50 °C and 90 °C (left to right); averaged values in colour, COV in grey.

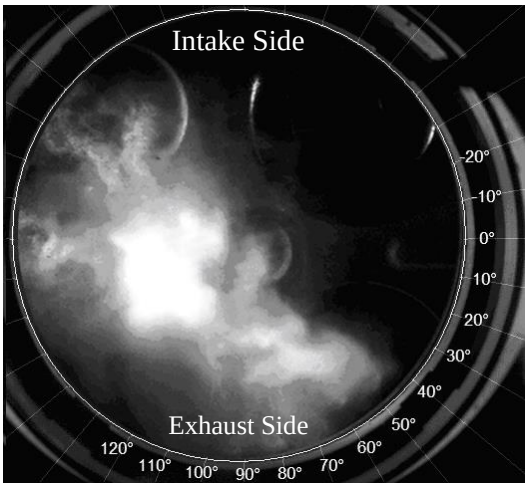


**Fig. 14.** Spray Image in Motoring Engine Overlaid with Polar Schematic of Sampled Heat Flux Locations around Cylinder Liner (*iso*-Octane, 20 °C, 10° CA ASOI, 1500 RPM, 1.0 bar Intake Pressure; intake valves: top, exhaust valves: bottom).

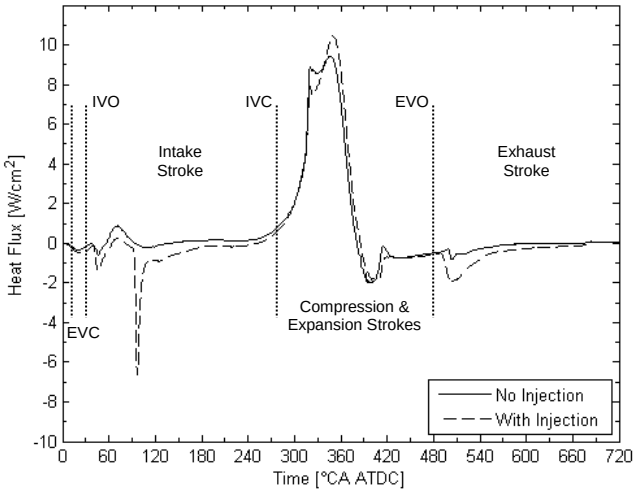


**Fig. 15.** Mean Heat Flux Signals for Motoring Engine with and without Fuel injection.

*iso*-Octane

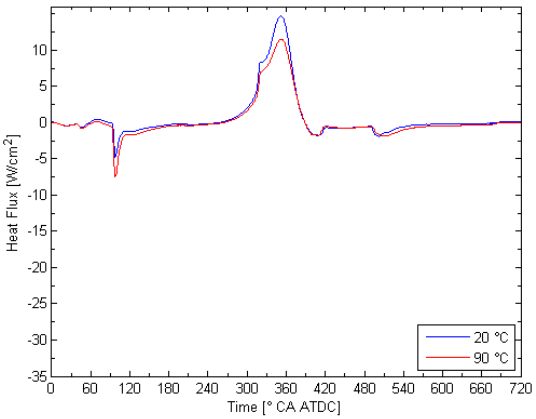


Gasoline

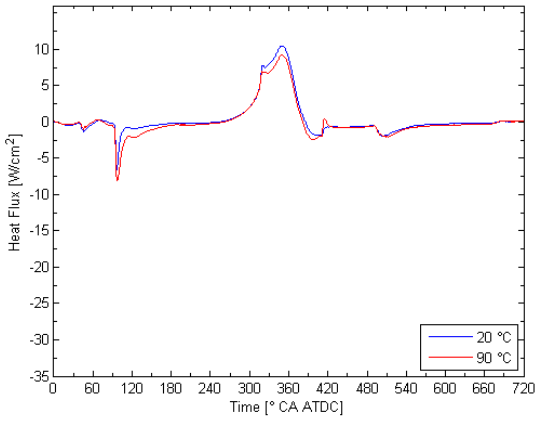


E10

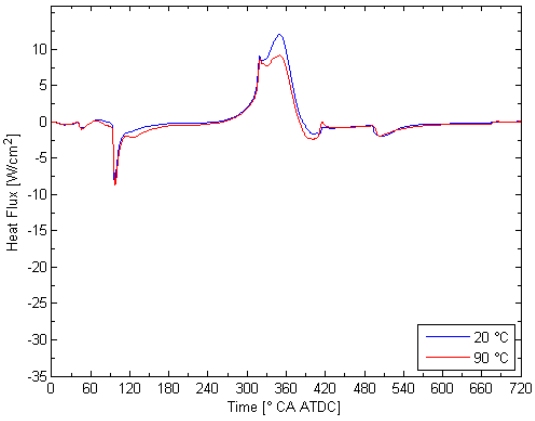


Ethanol

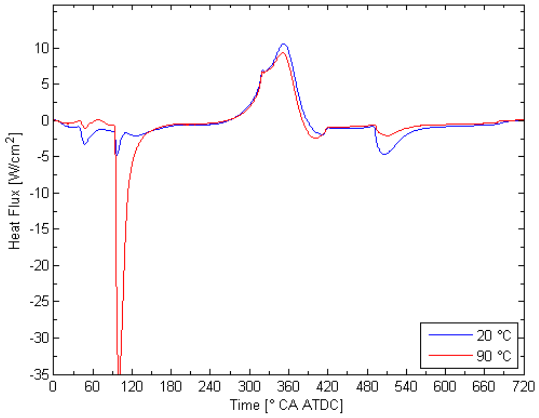


Butanol

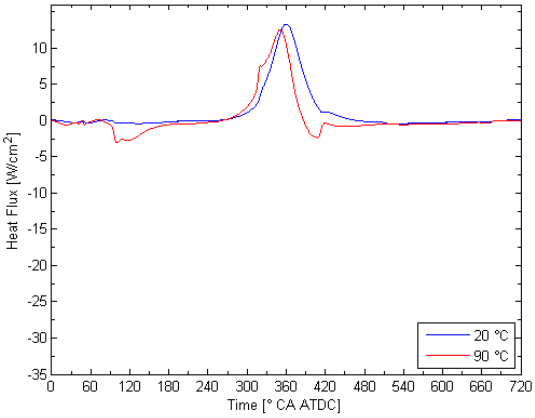


**Fig. 16.** Mean Heat Flux Signals for Different Fuel Types and Temperatures (Motoring Engine).

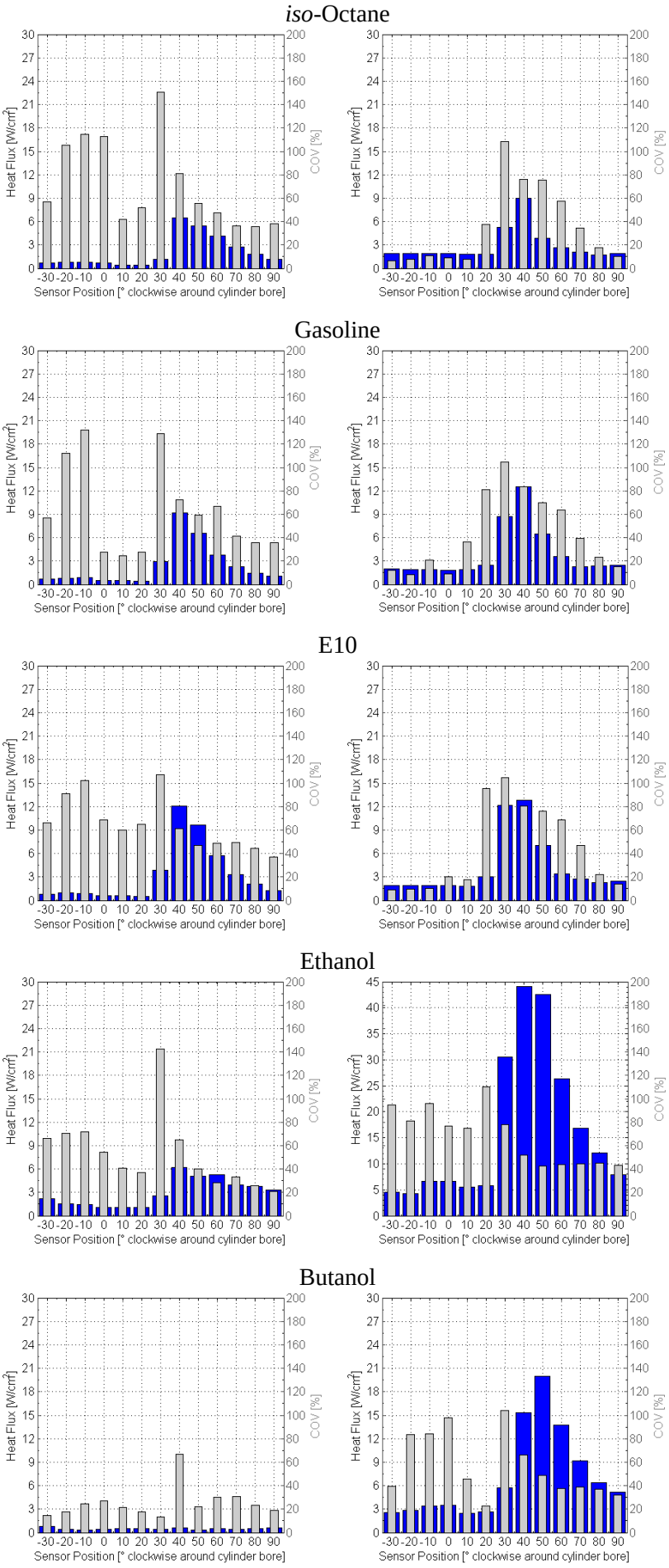


**Fig. 17.** Peak Heat Flux at Various Peripheral Locations for 20 °C (left) and 90 °C (right), 1.0 bar Inlet Pressure, 1500 RPM; averaged values in colour, COV in grey.